Aminophosphonate CuO nanocomposites for uranium(VI) removal: Sorption performance and mechanistic study

Enas Imam, Ahmed Hashem, Ahmad Tolba, Mohammad Mahfouz, Ibrahim El-Tantawy El-Sayed, Hamada Hawash, Rana Neiber, Hamed Mira, Ahmed Galhoum, Guibal Eric

Aminophosphonate CuO nanocomposites for uranium(VI) removal: Sorption performance and mechanistic study

Enas A. Imam [a], Ahmed I Hashem [b], Ahmad A. Tolba [a], Mohammad G. Mahfouz [a], Ibrahim El-Tantawy El-Sayed [c], Hamada B. Hawash [d], Rana R. Neiber [c], Hamed I. Mira [a], Ahmed A. Galhoum [a,*], Eric Guibal [e]

[a] *Nuclear Materials Authority, P.O. Box 530, El-Maadi, Cairo, Egypt*
[b] *Chemistry Department, Faculty of Science, Ain Shams University, Cairo, Abassia, Egypt*
[c] *Chemistry Department, Faculty of Science, Menoufia University, Shebin El-Kom, Egypt*
[d] *Environmental Division, National Institute of Oceanography and Fisheries, NIOF, Cairo, Egypt*
[e] *Institut Mines Telecom – Mines Ales, Polymer Composites and Hybrids, 6 avenue de Clavières, F-30319 Alès cedex, France*

A B S T R A C T

Two aminophosphonate matrices (mono-aminophopshonate, MAP, and bi-aminophosphonate, BAP) are syn-thesized, varying the molar proportions of three precursors (thiocarbazide, p-phthalaldehyde, and triphenyl-phosphite). Nano-composites (CuO-MAP and CuO-BAP) are successfully elaborated by impregnation of the matrices with copper sulfate solution before processing to *in situ* precipitation of copper in alkaline solution (simultaneous partial Cu reduction). The sorbents are characterized using: TEM, XRD, elemental analysis, SEM- EDX, BET, titration (pH_{PZC}), XPS and FTIR analyses. Uranium sorption properties are compared for the different sorbents through the study of pH effect (optimum close to 4.5), the uptake kinetics (equilibrium reached in 60 min) and sorption isotherms. Uptake kinetics are finely fitted by the pseudo-second order rate equation (and the resistance to intraparticle diffusion). The sorption isotherms are modeled by the Langmuir equation with maximum sorption capacity (mmol U g^{-1}) decreasing according to CuO-BAP(1.15) ≫ CuO-MAP(0.80) > BAP (0.74) ≫ MAP(0.50). The enhanced textural properties and the increase in the density of sorption sites (probably completed by a better steric arrangement for improved reactivity) may explain this ranking. The sorption is endothermic: sorption capacity and affinity coefficient increase with temperature. Uranium is readily desorbed from loaded-sorbents (efficiency > 98 %) using either HCl (0.2 M) solution or acidified urea (0.25 M) solution (pH 2.5) for aminophosphonate matrices and nano-composites, respectively. The type of sorbent does not affect the stability at recycling: at the sixth cycle, the loss in sorption and desorption performances varies by 6.2–7 % and 4.2–4.9 %, respectively. CuO-BAP sorbent shows high potential for uranium recovery from complex acid ore leachate. The broad spectrum of bound metals does not allow producing a pure yellow cake after ammonia precipitation of eluate (containing up to 15–22 % impurities).

Keywords:
Nanocomposites
Aminophosphonate functionality
Uranyl sorption
Regeneration studies
Application to uranium ore leachate

1. Introduction

Nuclear energy may be considered a clean power source in terms of climate change when compared with conventional fossil fuels [1–5]. In the coming years, it is expected to replace fossil fuels as the primary source of energy since it can continually produce massive amounts of electricity with extremely minimal greenhouse gas emissions [5,6]. The development of nuclear energy depends on the successful utilization of uranium, [3,7]. Hence, the uranium deposits are expected to run out within the next hundred years due to the rapid expansion of nuclear energy. In addition, uranium is a significant contaminant in radioactive wastewater; environmental regulations governing uranium release into the environment are getting more strict, which may be due to its intrinsic toxic effects, presence, and accumulating in the food chains. These considerations make effectively uranium resources utilisation (particularly low-grade minerals) and environmental preserving important challenges for uranium extraction and recovery from polluted water [8–11]. The use of adsorbents to extract uranium has been

* Corresponding author.
E-mail address: galhoum_nma@yahoo.com (A.A. Galhoum).

demonstrated to be an efficient way to exploit this inexhaustible resource [5,12,13], especially from dilute effluents. Therefore, different adsorbents have been synthesized to effectively remove uranium from contaminated water, including: biopolymers (i.e., chitosan, cellulose) [9,10,14], inorganic sorbents (i.e., mesoporous silica, clay minerals, metal oxides, metal–organic frameworks) [11,15,16], carbon- derived sorbents (i.e., graphene oxides, activated carbon) [8,9] and organic–inorganic hybrid composites [17,18]. As a hard acid uranium is a promotes to be bound to hard bases [10,19], according to Pearson theory (HSAB [20]). Therefore, extremely effective ligands for high capacity and selective uranium sorption include chelating resins containing reactive groups such as P O, N, and S [8,9,13,15]. Over the past ten years, organophosphorus compounds attracted a great interest., in relation with their applications in agriculture, pharmacology, biology, and medicine, as well as their broad use as synthetic intermediates [21]. Additionally, such these substances and their analogues are utilised in industry as chemicals for pollution control, metal removal, and water treatment. They are also good metal-complexing agents for many transition metals in therapeutic and diagnostic applications [15,22,23].

Organophosphorus compounds, such as α-aminophosphonates, mimic -amino acids structurally in that the carboxylic group is replaced with a phosphonic acid or equivalent moiety [22]. This similarity can explain their high reactivity and numerous applications. They are frequently used as ligands in transition-metal and organocatalysis [24,25]. The P=O moiety showed an effective coordination behavior with U(VI), according to studies on uranium removal utilising TBP (tributyl phosphate) and TRPO (trialkylphosphine oxides) [26]. The hydrolytic stability of the C-P bonds in the -aminophosphonate group also influences the synthesis of stable bioactive phosphate analogues [27]. However, in accordance with this kind of chemical structure, new materials that have particular functions, good extraction properties, and high stability are still required. It is also important to put into practice a comprehension of how the grafted-on ligands substitutions may enhance or decrease sorption efficiency in order to wide their practical use. Recently, it has been proposed that a viable method for creating highly selective sorbents with high reactivity and enhanced sorption performance consists in using multi-functional resins, bearing reactive groups such as thiocarbonyl, amino, phosphonate, or carboxymethyl moieties [28–31]. The advantages of the multifunctional materials include: higher sorption capacities caused by an increase in reactive group'-s content; selectivity produced by the interaction of vicinal functions and the optimum pH range for maximal sorption [10,30]. Several aminophosphonate sorbents have been previously developed and tested for their ability to bind to uranium [9,10,13,14,19,32], rare earth [33], and heavy metals [23]. The effects of induction, acid-base characteristics, steric hindrance or dual functions can all have a significant impact on the phosphonate moieties reactivity in multifunctional sorbents [34–36]. In addition, altering the molar ratios of reacting substances throughout synthesizing may have an effect on the overall sorption characteristics of the sorbents as a result of the variations in the density (or number) of reactive moieties as well as their structural configuration in the final product.

Significant efforts have been focused on the creation of transition metal/metal oxide nanostructured materials due to their appealing physicochemical features [37,38]. Metal oxides (MOs) have received a great attention because of their high specific surface area, high mechanical and thermal stability. CuO NPs (Copper oxide nanoparticles) are particularly interesting due to their specific properties that led to their use in solar energy conversion devices, gas sensors, catalysis, batteries, and high temperature superconductors. CuO NPs and composites have been previously developed and evaluated for metal binding; Cu (II) oxide nanoparticles [39] and chitosan-CuO or -Cu(OH)$_2$ [40] were used as adsorbents for arsenic removal from water. Graphene oxide (GO)–CuO nanocomposites showed remarkable adsorption behavior towards Pb(II) and Cd(II) [41], while CuO nanorods were used for Pb(II) adsorption [42]. Sorbents were developed for U(VI) recovery based on CrO- polyamides and CuO-polyamides [43]. CuO NPs can be prepared using various chemical and physical procedures. However, these techniques have limitations, including the use of organic solvents, hazardous reducing agents, high temperatures and/or pressures [44]. Therefor a green synthetic procedure for CuO NPs through a simple precipitation method in greener environment would be of great interest; avoiding the presence of any inert gases. The claimed advantages of this procedure concern: (a) high pressure or hazardous chemicals are not needed., (b) limited requirements in terms of energy and temperature, (c) simplicity, (d) environmentally friendliness, and (e) low cost. High thermal and chemically stable composite materials are created by combining organic and inorganic precursors [45]. Composite materials are produced by mixing two or more materials with contrasting and/or complementary properties to create a product with distinctive properties (high surface area and high ion-exchange and adsorption capacity). Nanocomposites are multiphase material; one of them having nanosized dimensions [11,46]. Thus, fabrication of organic–inorganic functional hybrid nanocomposite is the art of designing novel multiphase nanomaterials for efficient uranium sorption (high capacity, selective separation, the thermal stability and fast kinetics, and being economical) [11,18,47]. Till now, there are no published studies on the synthesis of CuO-aminophosphonate based nanocomposites, the effect of CuO NPs incorporation on the physicochemical properties and the studies of their U(VI) sorption properties. Herein, two new α-aminophosphonate compounds are prepared using one-pot synthesis reaction; through the reaction between trimethylphosphite, thiocarbazide and p-phthalaldehyde using various precursor quantities. In a second step, two nanocomposites composed of copper oxide nanoparticles and aminophosphonate matrices are synthesized. The aminophosphonate matrices are first impregnated with copper sulfate solution; copper is physically absorbed and adsorbed onto the organic matrices. In a second step, the Cu-impregnated materials are immersed in an alkaline solution (NaOH solution) at room temperature. The *in situ* precipitation of copper is accompanied by a partial reduction of the metal. Initially, FTIR, XPS, XRD, BET, TEM, UV–visible spectroscopy, SEM-EDX analysis, TG/DTA, elemental analysis and titration are used to characterize the chemical properties and physicochemical structure of the materials. In the second part of this work, properties of uranyl sorption for the different materials are widely investigated through the study of experimental criteria including the effect of pH, uptake kinetics, and thermodynamic parameters (along with sorption isotherms). For six regeneration cycles metal desorption and sorbent recycling are investigated. Finally, the sorbents are compared for the recovery of uranium from ore sample along a succession of steps: ore leaching, pre-treatment (precipitation), sorption, elution, and precipitation of yellow cake.

2. Materials and methods

2.1. Materials

p-Phthalaldehyde, triphenyl phosphite, thiocarbazide and acetonitrile were obtained from Aladdin (Beijing, China). Copper(II) triflate (Cu(OTF)$_2$) was purchased from Innochem (Beijing, China), copper(II) sulfate ($CuSO_4{\cdot}5H_2O$, AR) was supplied by Alpha Chemika (Maharashtra, India), arsenazo III (A.R grade) was obtained from Fluka Chemie AG (Buchs, Switzerland), and the remaining chemicals were Prolabo products (VWR, Part of Avantor Group, Radnor Township, PA, USA) and were used as received. $(UO_2(NO_3)_2).6H_2O$ (Uranyl nitrate) (supplied by Sigma-Aldrich, Saint-Louis, MI, USA) was used to prepare the U(VI) stock solution (i.e., 1 g U L^{-1}, 4.20 mmol L^{-1}): uranyl salt (1.06 g) was dissolved in 3 mL concentrated H_2SO_4 (16.38 M), under heating before being diluted to a final volume of 500 mL with demineralized water. The stock solution was diluted with demineralized water to prepare the working solutions before use.

2.2. Synthesis of sorbents

2.2.1. Synthesis of aminophosphonate materials (BAP and MAP sorbents

Scheme 1 shows the suggested structures of the two sorbents and their synthesis route. Triphenylphosphite, p-phthalaldehyde (di-aldehyde) and thiocarbazide (as amine source) and triphenylphosphite with various molar ratios (i.e., (2:1:2) and (1:1:1)) were dissolved in CH_3CN (5 mL) for preparing BAP and MAP, respectively. The mixture was stirred at room temperature for 15 min before the Lewis acid catalyst was added immediately (i.e., copper(II) triflate, known as triflic acid, Cu $(TOF)_2$), with a dose corresponding to 20 % (w/w). After stirring (at room temperature) for 3 days [10], the final products were filtered and washed up with acetonitrile and then allowed to air-dry to give α-aminophosphonate derivatives; i.e., bis- and mono-aminophosphonate (AP) derivatives (BAP and MAP, respectively). The detailed synthesis pathway appears in Scheme S1 (Section A, in Supplementary Information).

2.2.2. Synthesis of CuO-aminophosphonate nanocomposites

For the nanocomposites synthesis, the materials were grinded below 37 μm (size fraction). The same procedure was used for synthesizing the two AP-based nano-composites. First, aminophosphonate-based materials (BAP and MAP, 1 g) were dropped into copper sulfate solution (10 mL, 0.9 M) under sonication for 90 min. In a second step, NaOH solution (40 mL, 2 M) was added to the previous suspension [48]. After mixing (at room temperature (i.e., 25 ± 1 °C)) for 3 h black, precipitates were obtained; consistently with previous observations in the synthesis of chitosan/copper-based sorbents [40]. Filtrated residues (CuO-BAP and CuO-MAP) were washed several times with demineralized water (to reach pH 7), and the air-dried samples were stored in a desiccator.

2.3. Characterization of sorbents

The detailed description of characterization procedures can be found in Supplementary Information (Section B), where is also reported the equipment used for these analyses. The morphology (and size distribution) of sorbent particles was characterized by SEM (and image analysis) while the CuO nanoparticles were analyzed by TEM (for morphology and size distribution). A drop of the solution was applied on the CCG (carbon coated copper grids) before being dried by water evaporation room temperature for the TEM analysis. JEOL JEM-1010 transmission electron microscope (TEM, Jeol Ltd., Tokyo, Japan) at 80 kV at Regional Center for Mycology and Biotechnology, Al- Azhar University, Egypt (RCMB) was used to obtain the electron micrographs. XRD was used for analyzing the crystalline structure of the aminophosphonate compounds, and their composites with CuO (comparing dried materials at 200 °C, and calcined nanocomposites at 700 °C). The XRD patterns were recorded on a Smart Lab X-Ray Diffractometer (Philips PW 3710/31, Philips, Eindhoven, Netherlands, now part of Malvern Panalytical, Spectrics Group), in the range 2θ = 5–75°, at room temperature. The textural properties were quantified by N_2 sorption and desorption isotherms (BET, BJH, and DFT methods). To calculate the total surface area as well as the pore volume for the materials, nitrogen adsorption–desorption isotherms were used (after 3 h of degassing at 60 °C) with a (Nova 3200) Quantachrome BET analyzer (Nova 3200), data being treated with TouchWin™, v. 1.2, Quantachrome Instruments, Boynton Beach, FL, USA). The specific surface area was determined using the BET technique, while the porous characteristics were determined of by the BJH method. Chemical properties were analyzed by FTIR and XPS spectroscopy methods to identify reactive groups and interpret their interactions with U(VI). Utilising the wavenumber range of 4000–400 cm^{-1}, the FT-IR spectra were collected using a 4100 Jasco spectrophotometer (with a resolution of 12 cm^{-1} and scan time of 16 s) (Jasco Corporation, Tokyo, Japan) by the KBr pellet method. the X-ray photoelectron spectroscopy analyses were carried out using Perkin Elmer PHI 5600 (Perkin Elmer Instruments, Waltham, MA, USA). Mg K_α (Al K_α) radiation source (200 W) was used to irradiate samples placed on indium sheets with 0.8 mm X-ray beam diameter and 1 mm analytical zone diameter. The materials chemical composition was performed by elemental analysis (and completed by semi-quantitative EDX analysis) before evaluating their pH_{PZC} values (by the pH drift method). To determine the elemental analysis (CHN), an automated CHNS analyzer (Vario EL III, Elementar Analysensysteme GmbH, Langenselbod, Germany) was used. The ESEM-EDX analyses were acquired at 25–30 kV accelerating voltage), 60–120 s (counting time) and 1–2 mm (beam diameter). Scanning electron microscopy was performed using an ESEM model Philips XL 30 (Eindhoven, Netherlands) fitted with an EDX device (energy-dispersive X-ray spectroscopy). The histogram plots (the particle size distribution) were created by Origin 2018 after tool distances estimating (by Foxit Phantom PDF) through the image analysis. Diffuse reflectance spectroscopy (UV–vis) was performed using a V-570 spectrometer (Jasco Corporation, Tokyo, Japan). Thermogravimetric analyzer (Shimadzu TGA-50), (Shimadzu Corporation, Kyoto, Japan) was used to evaluate The thermal stability of the sorbents. Temperature ramp had been adjusted to 10 °C min^{-1}.

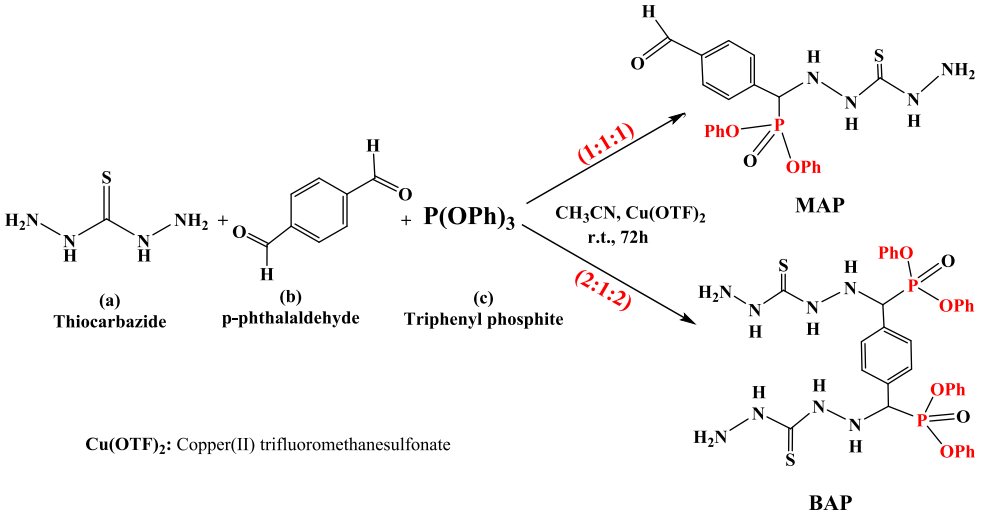

Scheme 1. The synthesis route of α-aminophosphonate sorbents (units of BAP and MAP).

2.4. Sorption and desorption procedures

In a batch system with fixed agitation (i.e., 200 rpm), Sorption and desorption experiments were performed. A specific quantity of the sorbent (m, 0.025 g) was mixed with a fixed volume of solution (V, 50 mL) at a particular initial pH value, pH_0 with C_0, 0.21 mmol (initial concentration) and sorbent dose (SD = m/V) of 0.5 g L^{-1}, unless specified (for example variable initial concentration for the study of sorption isotherms or the study of thermodynamics). (25 ± 1 °C) was set as the standard temperature. For uptake kinetics, at specified contacting times or at equilibrium, samples were gathered, filtered with a 2.5 μm pore size membrane filter and then analyzed to determine the $C_{(t)}$ or C_{eq}, (mmol U L^{-1}) (residual concentration). Also, the equilibrium pH was consistly registered. The so-called Arsenazo III colorimetric method was used to measure the uranium concentration [40]. A SP-8001 Metertech spectrophotometer (SP-8001, Metertech Inc., Taipei, Taiwan) was used to measure the absorbance at wavelength of 655 nm. The sorption capacity was calculated by ($q_{eq} = (C_0 - C_{eq}) \times V/m$) (the mass balance equation) and the (D (L g^{-1}): q_{eq}/C_{eq}) is corresponding to the distribution ratio. The sorption isotherms were performed at various initial concentrations varies between 0.12 and 1.28 mmol U L^{-1} at 0.5 g L^{-1} (SD) at pH_0 of 4.5 for 1 h under agitation of 200 rpm. For sorbent recycling and metal desorption, HCl (0.2 M) and acidified urea solutions (0.25 M, at pH 2.5) were used as the eluents for pristine sorbents and CuO sorbents, respectively; a contact time of 1-hour was needed for the metal desorption investigation. The sorption capacity obtained at the first step was compared to value at the sixth cycle. The desorption efficiency was also quantified using the mass balance equation. The graphs display averaging data (with standard deviation) from duplicated experiments.

2.5. Modeling of sorption phenomena

Conventional models were utilized to simulate the sorption results. PFORE (pseudo-first order), PSORE (pseudo-second order) equations and the resistance to intraparticle diffusion, RIDE (Crank equation) were used to fit the kinetic profiles for uptake kinetics. The Langmuir, Temkin, Sips, Freundlich and Dubinin-Radushkevich (D-R) equations were used to model sorption isotherms. The relevant conventional equations are summarized in Section C (see SI).

2.6. Ore treatment application

An ore sample obtained from El Allouga mining area (Southwestern Sinai, Egypt) was used for preparing leachate solutions. Geologic information and mineral composition is detailed in Section E (SI). Briefly, uranium content reaches 0.27 g kg^{-1}, while the major elements (81.5 %, w/w) are Fe, Ca, Si, Al, K, Na and Mg (as oxides) (Zn, Ti, Mn, Ti, Zn, Cu, Ni and Co are also present as trace oxides). Regarding uranium mineralization, it is noteworthy that the metal is present as U(VI) (readily soluble in primary minerals) and as U(IV) (poorly soluble in secondary minerals). The presence of MnO_2 (counting in the ore for 1.18 %, w/w), may be useful for oxidizing U(IV) and improving uranium leaching.

The ore was grinded and sieved below 100 mesh (i.e., <149 μm). Disposed in agitated tank, the ore was leached for 6 h at room temperature with a sulfuric acid solution (50 g L^{-1}), with a solid/ratio set at 1:4 (100 g in 400 mL). After filtering the leachate and washing the residue with demineralized water, a final volume of 400 mL of the leachate completed with washing solution was adjusted to prepare the pregnant leaching solution (PLS). A sample was collected (evaporated to 1/4) and analyzed for evaluation of element concentrations. The pH of the leachate was initially 1.67, to apply the sorption under favorable conditions; the pH was adjusted to 3.5–4. This pre-treatment step involves the precipitation of iron with some metal ions that are co-precipitated (including U); the precipitated leaching liquor solution (PPLS) was used for sorption tests. Operating conditions were set to time: 60 min; SD: 0.5 g L^{-1}; pH_0: 4.5 and 25 ± 1 °C (i.e., room temperature) under agitation of 200 rpm. The metal-loaded sorbents were desorbed using HCl solution (0.2 M) (for BAP and MAP sorbents) and 0.25 M acidic urea solution (with pH of 2.5); under experimental conditions correspond to: SD = 0.5 g L^{-1}, contact time = 60 min; v = 200 rpm, and T: 25 ± 1 °C.

The recovery of the yellow cake was processed by uranium precipitation as ammonium diuranate (adjusting the pH to 7.5, in the presence of ammonium hydroxide, 25 % w/w). After filtration and drying at 110 °C for 2 h, semi-quantitative EDX analysis was used for the yellow cake purity analyses.

3. Results and discussion

3.1. Sorbents synthesis

The synthesis procedure of α-aminophosphonates is reported in Scheme 1. The principle consists of one-pot synthesis reaction between thiocarbazide, p-phthalaldehyde and trimethylphosphite (varying the quantities of amine/phosphite precursors against p-phthalaldehyde) and using ($Cu(TOF)_2$) as a Lewis acid catalyst. The tentative structures of MAP (mono-substituted α-aminophosphonate) and BAP (di-substituted α-aminophosphonate) are reported in Scheme 1. Scheme S1 (in SI) proposed the successive mechanisms involved in the synthesis. The synthesis route includes first the synthesis of imine-intermediates. The imine intermediates are attacked in a second step by nucleophilic phosphite (electron-rich phosphorus) resulting in the phosphonium intermediate formation. The Lewis acid catalyst ($Cu(TOF)_2$) (i.e., Cu $(CF_3SO_3)_2$) catalyzed this step [40]. The target -aminophosphonates are produced after elimination of methanol by the reaction of water with phosphonium intermediates.

In a second step, CuO nanoparticles are generated *in situ* in the α-aminophosphonate matrix through copper impregnation (with copper sulfate solution) and precipitation with sodium hydroxide. While the reaction proceeds, a cloudy cluster of particles is formed. The formation of nanocomposites is associated with a notable color change [49]. The addition of sodium hydroxide into the copper sulfate pentahydrate solution makes the light blue color of copper sulfate solution turning to greenish-brown with maturation (here 3 h; consistent with copper oxide state). This color change is compatible with the results described by Elwakeel and Guibal [40] for the successive synthesis of chitosan/CuO and chitosan/$Cu(OH)_2$ composite sorbents. This is accompanied by a substantial pH change during the synthesis (up to pH 10.14 for CuO-BAP and 10.33 for CuO-MAP) already reported for manufacturing gold NPs [50] and producing silver NPs [51]. The water-washed particles were finally air-dried. It is noteworthy that the synthesis was performed in green environment (avoiding the application of inert gas and vacuum procedure). The detailed discussion of the mechanisms involved in the manufacturing of the composite is presented in Section A of Supplementary Material.

3.2. Characterization of materials

3.2.1. Physical characteristics

The majority of the sorbent particles observed by the SEM analysis are spherical and irregular in shape (Table S1). The average value of the particle sizes distribution is approximately 11.00 ± 4.73 μm for BAP (measured on 256 particles), 19.34 ± 8.89 μm for CuO-BAP (on 298 particles), 12.27 ± 5.78 μm for MAP (on 241 particles), and close to 12.38 ± 6.08 μm for CuO-MAP (on 179 particles).

The TEM micrographs of the nanocomposites (CuO-BAP and CuO-MAP) (reported in Table S2). Copper oxide NPs appear as irregular spherical structures with homogenous distribution, (though a slight agglomeration of NPs can be observed). This affirms that the nanoparticles are successfully incorporated within the aminophosphonate matrices. Tables S2 shows the TEM images of the composite sorbents, which are characterized by a core–shell structure. The core of the

composite is composed of the aminophosphonate fraction, partially coated by CuO nanoparticles. Also, the images revealed the heterogeneous surface of the nanocomposites and this could be used to show CuO role in increasing the surface roughness. For CuO-BAP, the average particle size stands to 9.06 ± 2.43 nm, little lower than for CuO-MAP (i.e., 11.79 ± 2.08 nm). It is noteworthy that the NPs have a narrow distribution. This range of particle sizes supports the qualification of sorbent particles as nanocomposites (size of nano-objects strictly below 100 nm).

As expected, the synthesis of the aminophosphonate compounds leads to the formation of amorphous structures: the XRD patterns are poorly resolved (Fig. S1a), especially for MAP. Apparently, the bis-aminophosphonation slightly improves the crystallinity of the final product: the symmetric phosphonate groups and the inter- or intra-chain interactions may lead to the formation of weak crystalline structure. The two sorbents (simply dried at 200 °C) show similar crystalline properties (which are better resolved than for raw materials). The incorporation of CuO (naturally crystalline) brings significant crystallinity to the nanocomposite. This is confirmed by a number of peaks appearing on both CuO-BAP and CuO-MAP materials: the majors peaks are observed at 2θ = 12.75°, 25.64°, 32.48°, 34.24°, 27.20°, 38.36°, 39.81°, 44.83°, 46.55°, 49.17°, 55.21°, 60.02°, 61.37° and 62.09°. The spectra of the two nanocomposites are roughly the same: CuO-AMP being better resolved; however, CuO-MAP shows supplementary peaks (such as at 2θ = 13.89°, 22.83°, or 53.5°) or more intense contributions (at 35.66°, for example). The composite XRD spectra include bands assigned to the material matrix and to the copper forms (including $Cu(OH)_2$ and/or CuO, [52,53]). It is noteworthy that the calcination at 700 °C drastically changes the XRD spectra of the sorbents: the thermal degradation of the sorbent matrix reveals the copper compounds, which are mostly formed

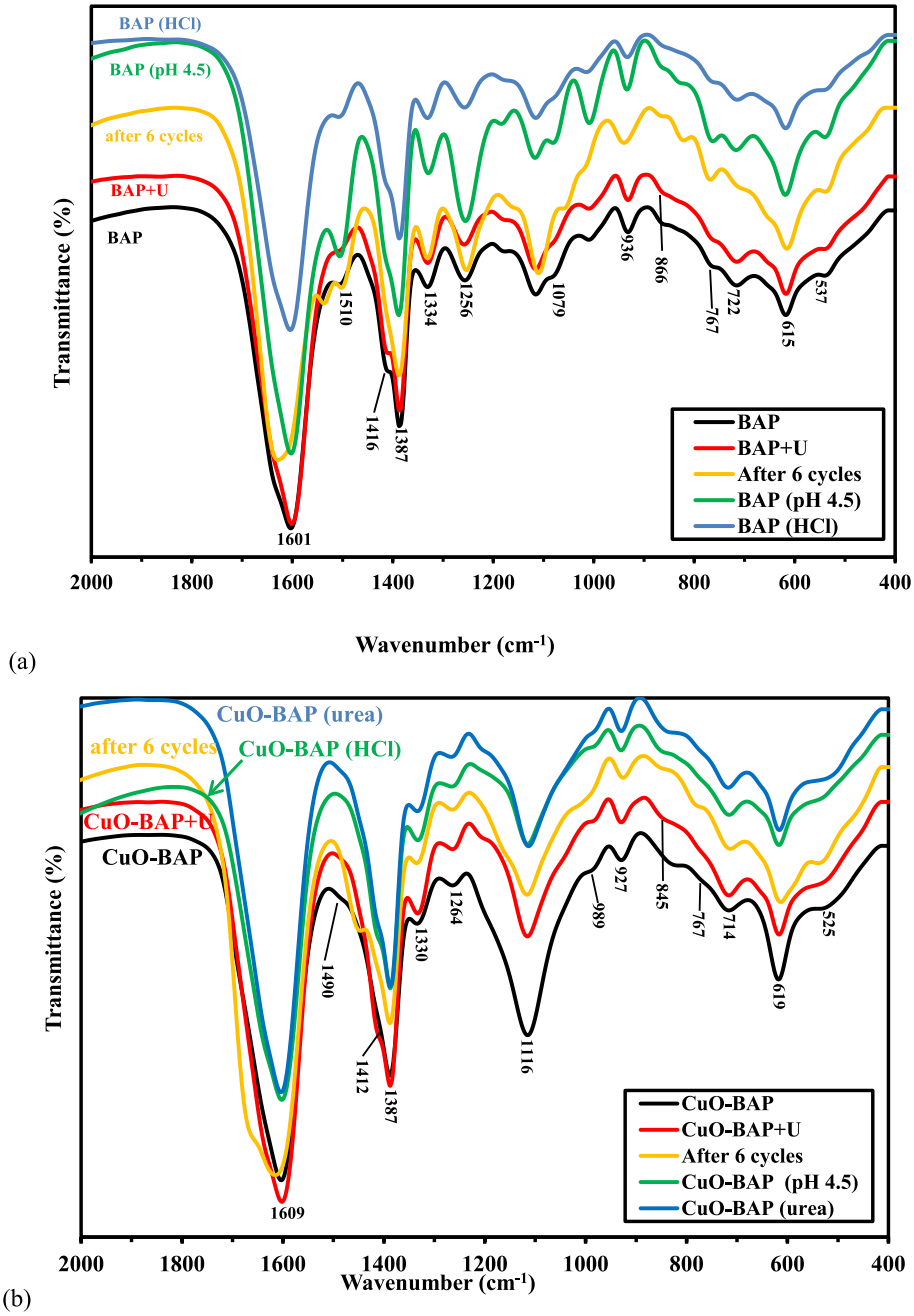

Fig. 1. Focused FTIR spectra of the four sorbents at different stages of use (pristine, after conditioning at pH 4.5, after U(VI) sorption, after conditioning in presence of urea, and after 6 cycles of reuse; wavenumber range 2000–400 cm^{-1}).

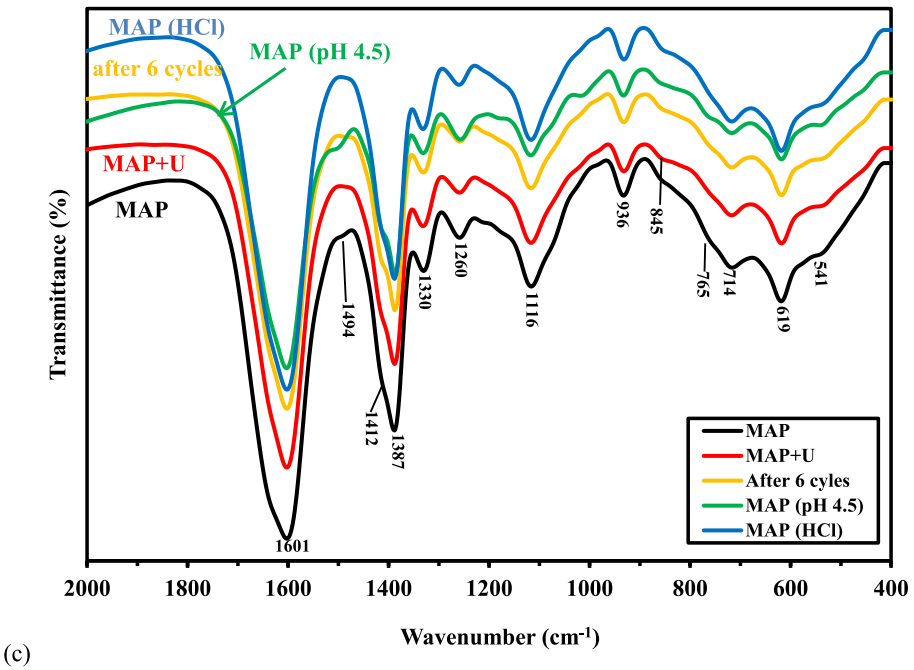

(c)

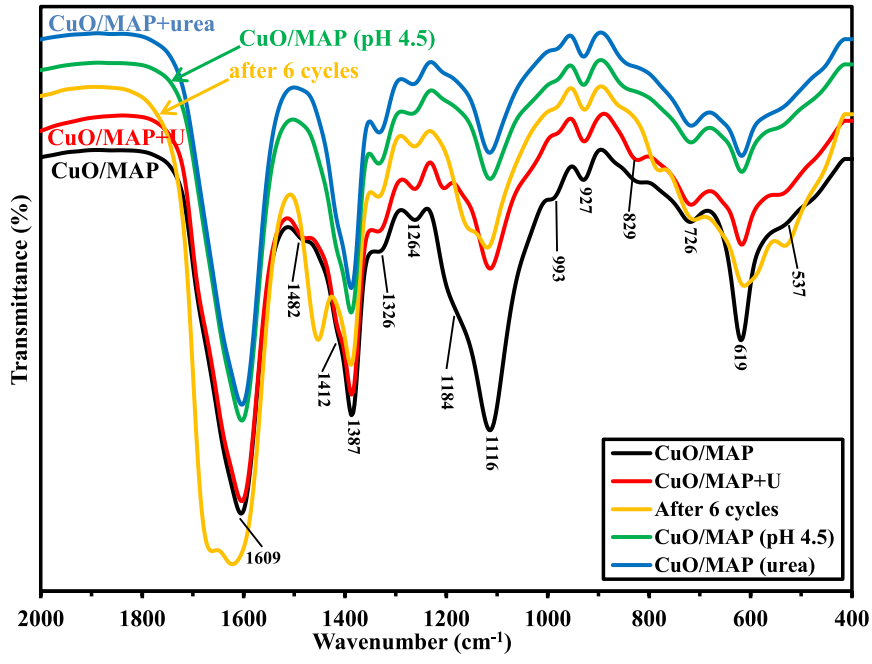

(d)

Fig. 1. (*continued*).

with CuO (and traces of $Cu(OH)_2$). Section A provides complementary interpretation of crystalline characteristics (more specifically focused on the existing forms of Cu-based compounds).

The N_2 sorption and desorption isotherms are all characterized by a marked convex shape (Table S3). This shape corresponds to Type III isotherm, which is associated to the fact that: (a) the monolayer is hardly identifiable, (b) the interaction adsorbent-adsorbate is weak, and (c) adsorbed molecules are clustered around the most favorable sites at nonporous or macroporous surface [54]. Another interpretation could associate the profiles to Type II isotherms with the completion of monolayer occurring at relative pressure (p/p_0) below 0.05: the gradual curvature is explained by the partial overlap of monolayer coverage and the onset of multilayer adsorption [54]. Based on BET results, the incorporation of CuO NPs increases the specific surface area: from 95.7 to 121.3 $m^2\ g^{-1}$ for BAP-based sorbent, and from 120.3 to 161.5 $m^2\ g^{-1}$ for MAP-based sorbents. As revealed from the TEM images (in Table S2), the heterogeneous surface of the nanocomposites could be used to show CuO role in increasing the surface roughness, and therefore enhanced the surface area. Nanoparticles offer to the sorbent the possibility to develop larger specific surface, while the bis-aminophosphonation reduces the surface of the composite sorbent (probably in reason of steric hindrance effects). Actually, MAP sorbent has S_{BET} value very close to the value obtained for CuO-BAP. The pore volumes are also strongly affected by the synthesis: BAP (0.410–0.407 $cm^3\ g^{-1}$) < MAP (0.422–0.424 $cm^3\ g^{-1}$) < CuO-BAP (0.465–0.481 $cm^3\ g^{-1}$)≪CuO-MAP (0.620–0.642 $cm^3\ g^{-1}$). The CuO-MAP sorbent shows remarkably higher pore volume than the three other sorbents: mono-aminophosphonation (combined with the incorporation of CuO NPs) opens larger pore space in the nanocomposite with higher dispersion and lower steric hindrance). The DFT method applied to N_2 sorption and

desorption isotherms shows that the four sorbents have roughly the same behavior in terms of pore size distribution (Fig. S2). Actually, the sorbents are characterized by bi-modal distribution of half pore width, with a first (smaller) contribution at ≈4 nm, and the larger contribution around ≈6.3 nm.

3.2.2. Chemical characteristics

The thermal degradation studies shows for raw materials three waves of weight loss successively related to the release of adsorbed water, the degradation of phenolic, methylphosphonate and amine groups [55], and the pyrolysis of the char (Fig. S3). The incorporation of phosphorous-based compounds is well-known for improving the fire-retarding properties of materials. Surprisingly, the sorbent bearing two aminophosphonate moieties is less stable to thermodegradation (weight loss reaching 92 % against 81.5 % for mono-substituted material). Obviously, the incorporation of CuO allows increasing the amount of residue (up to 66.6 % and 62.6 % for CuO-BAP and CuO-MAP, respectively). The profiles of degradation for the composite sorbents are superposed; however, above 450 °C the increase in aminophosphonate improves the stability of the composite.

The UV–visible reflectance spectra are recorded in Fig. S4. Similar profiles are observed in the range 200–400 nm, while above 400 nm large differences are detected with a translation to higher reflectance for pristine aminophosphonates compared with their CuO nanocomposites (following: BAP≫MAP ≫CuO-BAP > CuO-MAP). The intense absorption band around 215 nm is attributed to the $\pi \rightarrow \pi^*$ transition. The weak shoulder appearing at 300 nm is ascribed to the n-π^* transition [56]. Vijayakumar et al. [57] observed a similar UV absorption edge in the case of ZnO/CuO nanocomposite around 240 nm. Pristine sorbents show maximum reflectance at values ~83.1 % and ~62.9 % in the visible region (close to 800 nm) for BAP and MAP, respectively. Reflectance decreased to ~28.1 % and 25.3 % with incorporation of CuO nanoparticles in CuO-BAP and CuO-MAP, respectively. The reflectance decreases by 66–60 % after incorporation of CuO. Similar findings were also reported for ZnO/CuO nanocomposites [58].

The full-scale FTIR spectra of the materials at various steps of usage (pristine, after conditioning at the pH of sorption (i.e., pH 4.5), after U (VI) binding, and after six recycling steps) are reported in Fig. S5. The interpretation (based on Table S4) is discussed in Section B.7. Herein, the attention focuses on the wavenumber range 2000–400 cm^{-1}, and the main conclusions on the identification of reactive groups involved in U (VI) binding.

The aromatic ring of p-phthalaldehyde is identified at 2935–2915 cm^{-1} (stretching vibration) [23] and 1490–1410 cm^{-1} (aromatic C–H bending and/or aromatic C=C stretching) [23]. The main bands assigned to N-based compounds (amine groups, both primary and secondary) are identified within the range 3460–3200 cm^{-1} (stretching) [59,60]; 1610–1600 cm^{-1} (bending) [19]. The presence of S-based moiety (i.e., C=S) is authenticated by the band observed at 1335–1325 cm^{-1} [61]. Numerous bands attest to the presence of phosphonate groups: stretching at 1260–1250 cm^{-1} (–P=O) [10], stretching at 1116–1079 cm^{-1}, 940–931 cm^{-1} and 546–529 cm^{-1} (P–O–C) [32,62]. On the other side, the mineral fraction (i.e., CuO and related compounds) can be confirmed by the band at 993–981 cm^{-1} (Cu–O bending). These signals confirm the successful grafting of precursors and the incorporation of CuO.

Significant shifts are observed with additional peaks after U(VI) binding which affects the functional groups environment [14,23]; the absorption intensities of –NH and $–NH_2$ groups relatively increased in the region at 3456–3420 cm^{-1}. In addition, the peaks correlated to vibrations of υ(P=O), υ(P–O–C) and υ(P–CH) at 1264–1256, 936–927 and 767–761 cm^{-1} are displaced after U(VI) binding with relative intensity decrease [19]. It is noteworthy that the peak located at 1184 cm^{-1} specified to the δ(C–H) (in conjugated aldehyde) in mono-sorbents is displaced to 1180 cm^{-1} and 1207 cm^{-1} in MAP and CuO/MAP, respectively. In the mono sorbent, along with the aldehyde group, relative contributions of phosphonate and amine groups are changed: these groups are included in U(VI) sorption. After metal binding, a new band located at 866–829 cm^{-1} corresponding to the vibration of O=U=O [63,64].

Also, the FTIR spectra of the materials were compared after six cycles of sorption and desorption to confirm the materials stability after recycling. Fig. 1 displays the FTIR spectra of the U(VI)-loaded materials after desorption that are partially recovered their initial spectra of the materials: the bands are shifted but differing from their original wavenumbers. Moreover, it is remarkable that numerous bands associated with uranyl sorption persist as traces in the spectra of regenerated sorbents. Actually, the spectra of regenerated materials are "intermediary" between those of pristine and metal-loaded sorbents. In particular, the set of bands from 3456 to 3420 cm^{-1} has been drastically decreased. Also, marked alterations occur in the area 1264–750 cm^{-1}, where the typical phosphonate bands can be recognized. This indicates that amine, phosphonate and aldehyde moieties have been affected by the sorbents regeneration.

The XPS survey spectra of CuO-BAP sorbent shows the most representative bands representative of functional groups: N 1*s*, C 1*s*, O 1*s*, P 2*p*, bands are tracers of both the organic phase (phosphonate moiety) and the mineral compartment (CuO and associated forms of copper). Copper is identified by a series of specific bands (i.e., Cu 3*p*, Cu $2p_{1/2}$, Cu $2p_{3/2}$, and Cu2*s*). Fig. S6b provides the HRES spectra of CuO-BAP before and after U(VI) sorption for signal Cu 2*p*. Cu^{2+}_{sat} is typically present in the analysis of CuO compound (but not appearing – or negligible – with Cu (0) and Cu_2O). The deconvolution of the Cu 2*p* signals in two components may be explained by the coexistence of two types of compounds: at 936.0 eV and 939.0 eV for Cu $2p_{3/2}$ and 955.1 eV and 957.8 eV for Cu $2p_{1/2}$, respectively. Lower BEs correspond to CuO while higher BEs are associated with $Cu(OH)_2$ form (or associated sulfate forms like in posnjakite or brochantite. The sorption of uranyl ions substantially changes the core-level spectrum of Cu 2*p* signal. (a) shifts in BEs (at 932.7 eV/935.0 eV, and 952.6 eV and 955.4 eV) and (b) inversion in the intensity of the two components for both Cu $2p_{1/2}$ and Cu $2p_{3/2}$. This means that the copper-compound contributes to uranyl sorption (modification of Cu environment). The deconvolution of U 4*f* signals (U $4f_{5/2}$ and U $4f_{7/2}$ doublet, also appearing in Fig. 6b) shows a major component at BEs (binding energies): ≈382.0 eV and 392.8 eV, respectively. This doublet is associated with the U(VI) form [65]. Another doublet is observed at BE values of 384.3 eV and 394.6 eV. This second doublet may be assigned to satellite peaks [65,66]; indeed, U(IV) are supposed to appear at lower BEs (i.e., 380 eV or below, [67]).

Table S5 reports the semi-quantitative EDX analysis of the materials (before and after uranyl binding). It is essential to keep in mind that EDX analysis is only applicable at depths of ≈2 μm); therefore, the reported compositions represent the surface of sorbent particles. This may explain the possible discrepancies with elemental analysis (Table S6). Table S6 summarizes the elemental analysis of the materials. The presence of N, P, and S elements attests to the effective grafting of precursors. The molar ratio N/P for the aminophosphonate fraction (4.39 for BAP and 4.51 MAP) is slightly higher than the expected 4:1 ratio; similar trend is observed for the N/S molar ratio (4.4 *vs.* 4). This means that the synthesis slightly diverges from theoretical reaction scheme. This can be explained by a slight degradation of C=S group and/or a weaker efficiency of triphenylphosphite immobilization, respectively. However, the global structure is relatively close to the suggested theoretical formula (determination coefficient close to 0.98 in the distribution of elements). The mineralization of composite sorbents allows analyzing copper content. Surprisingly copper content is significantly higher for CuO-BAP (i.e., 17.2 %, w/w) than for CuO-MAP (i.e., 11.6 %, w/w). This could explain that despite a weaker thermal stability of BAP (compared with MAP), the amount of residue at 800 °C is greater for CuO-BAP (than for CuO-MAP, Fig. S3). Also, these results are less than that obtained by the EDX analysis of the composite sorbents surface (25.1 % for CuO-BAP *vs.* 18.4 % for CuO-MAP). This could indicate that the distribution of

CuO nanoparticles is not homogeneous in the sorbents. The mode of impregnation favors the accumulation of copper in the external layers of the sorbent; after *in situ* precipitation, a concentration gradient may exist in the distribution of copper oxide forms.

The pH-drift method was used to determine the pH_{PZC} values of the sorbents. Fig. S7 shows that the pH_{PZC} values are not significantly changed by the number of aminophosphonate groups: 2.94 and 2.72 for MAP and BAP, respectively. The first acidity of aminophosphonate strongly varies with the substituents hold on the compound; in most cases, the pK_a varies between 2 and 2.9 [68]. This is consistent with the values reported herein. Similar values were cited for aminophosphonate functionalized poly(glycidyl methacrylate) [69], while the aminophosphonation of chitosan leaded to pH_{PZC} values close to 6.24 for methylphosphonate derivative and to 3.13 for the phenylphosphonate derivative [10]. The difference in the acid-base properties were explained by the strong negative inductive effect (-I) of phenyl groups and the steric hindrance impact (compared with methyl groups). The present results are consistent with the values reported for chitosan functionalized by the aminophosphonation bearing phenyl groups (as herein). The alkaline properties of amine groups (and C=S) are not significantly influencing the acid-base properties of synthesized sorbents. It is noteworthy that at pH inferior to 2.7–2.9, BAP and MAP are positively charged; the metal cations may be provoked as a result of the reactive groups protonation. It is supposed that pH > 3 (with deprotonation of functional groups) will be more favorable for metal binding. The incorporation of CuO drastically increases the pH_{PZC} values of composite sorbents up to 6.43–6.95. This may be explained by the presence of CuO (and associated copper hydroxide forms, though less present than the CuO form) and by the effect of Cu(II) binding during the impregnation step of the synthesis procedure, which may affect the functional groups acid-base properties. Obviously, this change in the pH_{PZC} values strongly affects the possible interaction of the sorbent with metal cations in the solution as well as its surface charge. It is anticipated that the pH-edges for favorable sorption will be shifted toward higher pH values after incorporation of CuO.

3.3. Sorption studies – Synthetic solutions

3.3.1. pH effect

The sorption of uranium is strongly influenced by the pH (Fig. 2). At acidic pH values (below pH 2), the binding capacities remain below

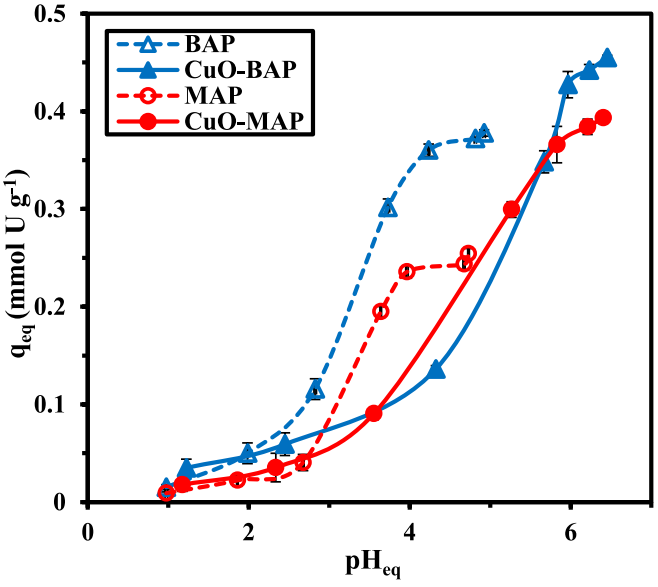

Fig. 2. Effect of pH on U(VI) sorption using selected sorbents (C_0: 0.21 mmol U L^{-1}; Sorbent dose, SD: 0.5 g L^{-1}; v: 200 rpm; time: 60 min; T: 25 ± 1 °C).

0.04 mmol U g^{-1} for MAP and CuO-MAP and below 0.06 mmol U g^{-1} for BAP and CuO-BAP. Under these conditions, the incorporation of CuO does not influence uranium sorption; and the reactivity of reactive groups for metal binding is limited by their protonation. However, the increase in the density of reactive groups (in BAP-based sorbents) slightly enhances metal uptake. With the pH increase, the reactive group's protonation gradually diminishes and sorption capacity sharply increases for BAP and MAP sorbents up to pH_{eq} 4–4.5 and stabilizes up to pH_{eq} 4.8–5.

In the case of CuO-composite sorbents, the increase in the sorption capacity slightly rises up to pH_{eq} 3.5; the sharp increase in the pH-edge is shifted toward higher pHs (compared with non-composite materials).

Fig. S8 shows the U(VI) speciation in the solution. The solution being prepared in sulfuric acid solution, uranyl is predominant under the neutral $UO_2SO_{4,aq}$ form (about 60 %) at pH below 2, associated with anionic and cationic species (i.e., free UO_2^{2+} and $UO_2(SO_4)_2^{2-}$, respectively) (Fig. S8). Therefore, the sorption of U(VI) under acidic conditions may be explained by the binding of $UO_2(SO_4)_2^{-}$ onto protonated amine groups; although the competition of protons reduces the capacity of the sorbent. The weak increase in sorption for BAP-based sorbents can be explained the little increase in N- and P-contents. Above pH 2 and up to pH 4.5, free uranyl species predominate; these species are more favorable for metal binding onto deprotonated reactive groups (i.e., amine groups) from the sorbent but also for the binding on phosphonate moieties. Above pH 4, the forming of hydrolyzed forms (UO_2OH^{+}) and polynuclear forms (such as $(UO_2)_4(OH)_7^{+}$) $(UO_2)_3(OH)_5^{+}$, $(UO_2)_3(OH)_4^{2+}$, $(UO_2)_2(OH)_2^{2+}$), complicates the understanding of the sorption mechanisms. Above pH 5, the formations of hydrocolloids (based on polynuclear hydrolyzed uranyl species) and precipitate lead to the overestimation of sorption performances. The precipitation contribution compensates (and overpasses) the decrease in the sorption of polynuclear hydrolyzed uranyl species (which is due to the necessity to operate hydroxyl exchange, and to the effect of limitation to diffusion of large size metal ions and access to core reactive groups). For this reason, pH 4.5 was selected for further studies.

Based on the differences in pH_{PZC} between composite and free aminophosphonate compounds, a special attention must be paid to pH variation during the sorption process. Fig. S9a confirms that the two "families" of sorbents follow different trends. For composite materials (with higher pH_{PZC} values), the equilibrium pH systematically increases, especially at pH_0 higher than 2. The variation of pH may reach up to 1.6 pH unit. Therefore, the equilibrium pH corresponds to conditions of possible precipitation of uranyl hydrolyzed species. This can also explain the high sorption capacity observed with composite materials; metal removal may result from the combination of sorption and precipitation mechanisms. This phenomenon can be correlated with the XPS analysis of CuO-BAP sorbent before and after uranyl binding: the relative proportions of the two peaks representative of Cu 2*p* signals are reversed after metal sorption. This can be explained by the contribution of copper in U(VI) binding and/or the alteration of copper's chemical environment (instability and pH change). On the opposite hand, in the case of pristine aminophosphonate compounds the pH tends to weakly decrease (by less than 0.6 pH unit, except at pH_0 6, where pH variation reaches 1.1–1.3 pH unit). In this case, the pH variation is only due to the effect of the organic compound: the release of protons (resulting from proton exchange during metal sorption) and/or hydrolyzed species binding (consuming hydroxyl groups for formation of hydrolyzed polynuclear species) contribute to the pH decrease, depending on the pH region.

Fig. S9b plots the decimal logarithm of the distribution ratio *vs* equilibrium pH (BAP-based and MAP-based series are joined in the linear regression analysis). The slope of the four series (not shown) varies between +0.44 and +0.56; the combined series gives a slope close to 0.51 for BAP-based sorbents, while for MAP-based materials the slope is about +0.45. The slope is related to the stoichiometry of exchange of protons in ion-exchange mechanisms,. Herein, the stoichiometric ratio is close to two protons (from protonated amine groups and phosphonate

moieties) per bound uranyl.

3.3.2. Uptake kinetics

Fig. 3 compares he uptake kinetics. The equilibrium is reached within 60 min under specific experimental conditions. The equilibrium concentrations are consistent with the trends observed in the pH effect study. The initial slope becomes steeper according to the series: MAP≪BAP < CuO-MAP≪CuO-BAP. The mass transfer is favored by the incorporation of CuO, consistently with the enhancement of textural properties (more specifically the BET specific surface area). The faster initial sorption is explained by the increased reactive group's density (N- and P- sites). The resistance to bulk, film, and intraparticle diffusion (diffusion mechanisms) as well as the proper reaction rate control the uptake kinetics. The resistance to bulk diffusion can be ignored by appropriate agitation (see Fig. S10).

Typically, the resistance to film diffusion becomes active within the first minutes of contact (corresponding to the initial slope of the concentration decay curve); its effect can be minimized by appropriate agitation speed (herein 200 rpm). The resistance to intraparticle diffusion is especially active in the case of poorly porous materials; this effect can be increased for large-size solutes (this may be the case for polynuclear hydrolyzed uranyl species). This step is responsible for delayed equilibrium time. The PFORE (pseudo-first order rate) and PSORE (pseudo second order rate) equations can be used for modeling the proper reaction rate. With reference to homogenous chemical reactions, the relevant equations were successfully applied to heterogeneous systems. However, under these circumstances the variables could be regarded as obvious rate coefficients which inherently take into consideration the participation of the resistance to diffusion. Table S7 summarizes the equations of PFORE and PSORE, in addition to the Crank equation (simplified equation used for modeling the intraparticle diffusion resistance, RIDE). Table 1 displays the comparison of Akaike Information Criterion values (AIC) and the determination coefficients for the three models and the different sorbents which demonstrates that the PSORE provides the best fit for experimental profiles. This is compatible with the results reported by Imam et al. [10] for aminophosphonate functionalized chitosan. The difference in AIC values is considered significant when $|\Delta AIC|>2$. The statistical variables match RIDE and PSORE. In Fig. 2, the experimental profiles (represented by the solid lines) are fitted by the PSORE; the fits with the PSORE and the RIDE are represented in Fig. S10. The fit of uptake kinetics by the PSORE is frequently interpreted as a system controlled by chemical sorption. However, Hubbe et al. [70] discussed this short cut in the interpretation of kinetic modeling. They reported a series of conditions that must be fulfilled to validate this conclusion. One of the most critical and rarely satisfied conditions concerns the "invariability" of the solution concentration (this correspond to "infinite volume" conditions). Herein, the

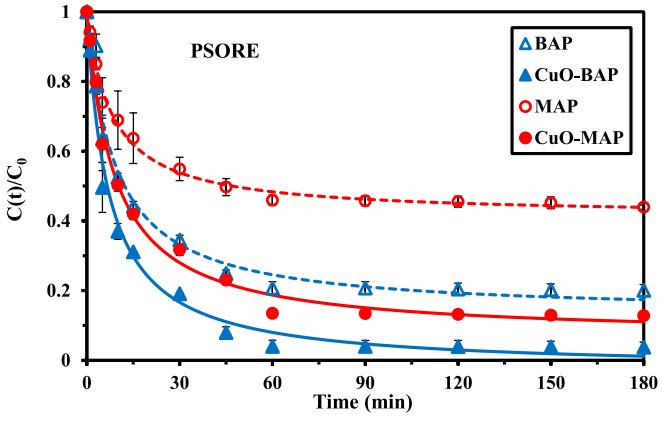

Fig. 3. U(VI) uptake kinetics using selected sorbents – Modeling with the PSORE (C_0: 0.22 mmol U L^{-1}; pH_0: 4.5; SD: 0.5 g L^{-1}; v: 200 rpm; T: 25 ± 1 °C).

Table 1
U(VI) uptake kinetics – Parameters of the models.

Model	Parameter	Unit	Sorbent			
			BAP	CuO-BAP	MAP	CuO-MAP
Exper.	$q_{eq,exp.}$	mmol U g^{-1}	0.357	0.430	0.250	0.389
PFORE	$q_{eq,1}$	mmol U g^{-1}	0.350	0.420	0.239	0.377
	$k_1 \times 10^2$	min^{-1}	8.60	10.6	9.05	8.48
	R^2	–	0.981	0.980	0.981	0.981
	AIC	–	−78	−73	−88	−76
PSORE	$q_{eq,2}$	mmol U g^{-1}	0.387	0.458	0.262	0.417
	k_2	g $mmol^{-1}$ min^{-1}	0.288	0.314	0.471	0.270
	R^2	–	0.981	0.987	0.994	0.993
	AIC	–	−78	−79	−105	−91
RIDE	$De \times 10^{13}$	m^2 min^{-1}	1.50	1.28	3.31	1.28
	R^2	–	0.981	0.985	0.994	0.994
	AIC	–	−78	−72	−106	−90

variation in solution concentration is large enough to invalidate the interpretation of chemisorption mechanism. They also concluded that in most cases when the conditions are satisfied, the experimental profiles fitting with the PSORE corresponds to a system controlled by resistance to intraparticle diffusion. This is definitively in consistence with the close values tabulated in Table 1, where the statistical variables are consistent with PSORE and RIDE. At equilibrium, the estimated sorption capacity ($q_{eq,2}$) overestimates the empirical values of sorption capacity at equilibrium by 4.8–8.4 %; the PFORE underestimates these values (by 2–4.4 %). The experimental sorption capacities at equilibrium are in consistence with the patterns identified by the pH study: CuO-BAP > CuO-MAP > BAP≫MAP. The apparent rate constants (k_2, g $mmol^{-1}$ min^{-1}) are in the same range for the different systems (i.e., 0.27–0.47 g $mmol^{-1}$ min^{-1}), varying according the series: MAP≫CuO-BAP > BAP > CuO-MAP. This ranking diverges from the trends observed in the initial slope of the curves (Fig. 2). The order of magnitude agrees with the results reported by Imam et al. [10] for two derivatives of chitosan (functionalized with aminophosphonate compounds) (i.e., k_2: 0.10–0.48 g $mmol^{-1}$ min^{-1}). Galhoum et al. [69] obtained higher apparent rate coefficient for U(VI) sorption using PPA-PGMA/Fe_3O_4 sorbent (i.e., k_2: 1.24 g $mmol^{-1}$ min^{-1}).

In Table 1, the values of D_e, m^2 min^{-1} (i.e., the effective diffusion coefficient) are reported for the different sorbents. The four sorbents are characterized by diffusion coefficient ranging in an equal order of magnitude (i.e., 1.28–3.31 × 10^{-13} m^2 min^{-1}). the uranyl free diffusivity in water (i.e., 4.56 × 10^{-8} m^2 min^{-1}, [71]) is numerous orders of magnitude higher than these values. This gap clearly demonstrates that the intraparticle diffusion resistance participates in controlling the global mass transfer in the U(VI) sorption of by the different sorbents. Within weakly acidic solution, Venkatesan et al. [72] reported for a macroporous bifunctional phosphonic acid resin a diffusivity coefficient of U(VI) near to 6.3 × 10^{-10} m^2 min^{-1}. In the case of TBP-impregnated sorbent, the diffusion coefficient was evaluated near to 1.0 × 10^{-10} m^2 min^{-1} [73]. Also, the results reported by Galhoum et al. [69] (i.e., 3.4 × 10^{-9} m^2 min^{-1}) are several orders of magnitude higher than the current diffusivity coefficient. A solution for enhancing the intraparticle diffusion was recently reported by Wen et al. [74]: the application of ultrasound doubled the diffusion coefficient. They explained this enhancement by several effects: cavitation, fast and strong rise in the local temperature, and the high-speed micro flow in the porous network. Herein, the positive influence of temperature increase on sorption performance (see next section) let anticipating a similar improvement of mass transfer properties using ultrasonic treatment.

3.3.3. Sorption isotherms and thermodynamics

Under fixed conditions of pH (herein pH 4.5) and temperature, the sorption isotherms represent the solute distribution between solid phases and liquid, at equilibrium. Fig. 4 shows uranyl sorption isotherms

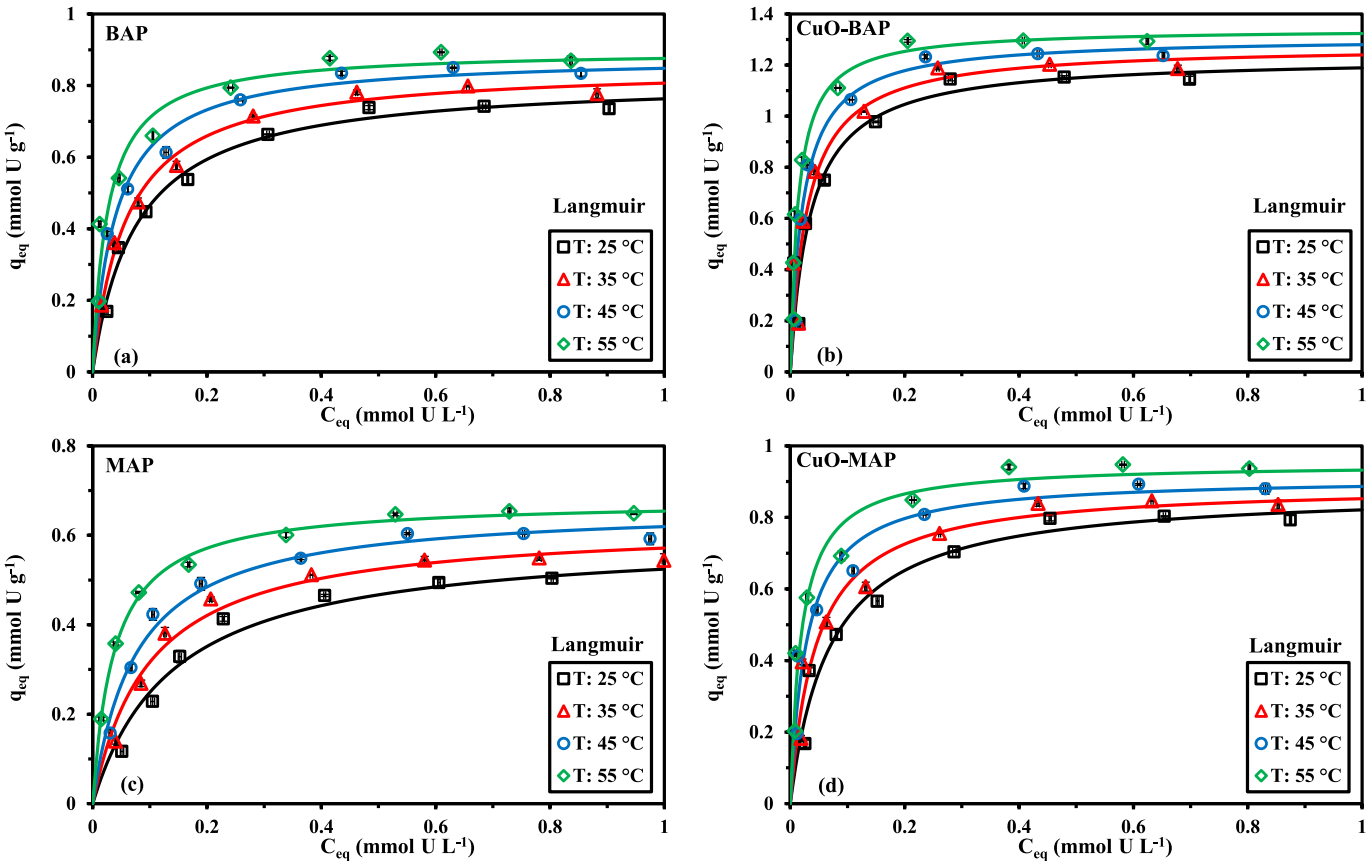

Fig. 4. U(VI) sorption isotherms using selected sorbents (a: BAP, b: CuO-BAP, c: MAP, and d: CuO-MAP) at different temperatures – Modeling with the Langmuir equation (C_0: 0.112–1.27 mmol U L^{-1}; pH_0: 4.5; SD: 0.5 g L^{-1}; v: 200 rpm; time: 60 min).

obtained with the different sorbents at temperatures 25 ± 1, 35 ± 1, 45 ± 1, and 55 ± 1 °C. The curves can be described by a steep initial slope followed by an asymptotical trend related to the sorbents saturation plateau. The sorbent's affinity for the solute is represented by the curves' initial slope, while the plateau may be associated with the monolayer saturation (in the Langmuir model). The sorbents can be ranked, regarding maximum sorption capacities, according to the series: CuO-BAP≫CuO-MAP > BAP≫MAP.

In addition, the temperature has a strong effect on the sorption isotherms that is indicated by the initial slope (i.e., ≈affinity coefficient) and the maximum sorption capacity increase with temperature. These trends indicate that the sorption is endothermic. This will be analyzed below.

To evaluate the relative contribution of the mineral compartment (CuO-based material), complementary U(VI) sorption tests were performed with two Cu–O based sorbents. Copper sulfate solution was precipitated as Cu(OH) (blue color solid) using NaOH solution until reaching pH 11.5. The first CuO-based sorbent (CuO(7 0 0)) was obtained by calcination at 700 °C for two hours. The second CuO(1 0 0) was synthesized by the same procedure used for the synthesis of the current sorbents (except that the aminophosphonate compounds were not added). This material was dried at 100 °C overnight (turning into CuO, due to thermodynamic instability). These two materials were tested for U(VI) sorption under fixed experimental conditions (i.e., pH0 4.5; SD: 0.5 g L-1; contact time: 60 min, at room temperature; i.e., 26 °C.

Different conventional equations were tested to fit the experimental profiles. The relevant equations for the sorption isotherms are reported in Table S8. The mechanistic Langmuir equation assumes a monolayer sorption to occur at the sorbent surface with similar sorption energies (sorbent homogeneity) and without interactions amongst the adsorbed molecules.

The empirical equation (Freundlich) follows a power-type trend poorly consistent with systems involving saturation plateau (as in the current study); the sorption is assumed being heterogeneous with potential interactions amongst neighbor adsorbed molecules. The Freundlich and the Langmuir equations are combined in the Sips equation: the fit quality may be improved (in certain cases) by adding a third modifiable parameter that may, in certain cases, improves the quality of the fit (accompanied by a reduction in physicochemical significance). The Temkin equation assumes that the heterogeneous binding sites are uniformly distributed and with linear variation of their binding energies [75,76]. The Dubinin-Raduskevich (D-R) equation derives from modeling interactions between gases and solids; the modeling of gas–solid interactions. Compared with the Langmuir equation (monolayer covering of non-porous or macroporous structures), the mechanism involved in D-R considers that the binding operates by volume filling (microporous structure) [77].

At T: 25 °C (Table 2), the maximum sorption capacity increases by 44–47 % when the bis-aminophosphonate moieties is grafted (*vs.* mono-aminophosphonate), while the incorporation of CuO mineral compartment increases the $q_{m,exp}$ value by 55–59 %. Therefore, the increase in sorption capacity is not directly related to the number of reactive groups (Table S6). The steric arrangement of phosphonate moieties and amine groups (reactive groups) is probably more favorable for accommodating uranyl chelation in this configuration. Ye et al. [78] stated the high stability of the chelate between uranyl and bis-phosphonated ligands (polyaminophosphonate ligands) for the design of uranium decorporation agents. In most cases, the D-R and the Langmuir equations fit better experimental profiles (with the remarkable exception of the MAP isotherm, where the Sips equation finely fits the sorption isotherm). The fitting with the D-R equation allows reaching calculated sorption capacities (overestimated by + 7.7–11.7 %) closer from experimental

Table 2
U(VI) sorption isotherms (at T: 25 ± 1 °C) using selected sorbents – Parameters of the models.

Model	Parameter	Unit	Sorbent			
			BAP	CuO-BAP	MAP	CuO-MAP
Exper.	$q_{eq,exp.}$	mmol U g^{-1}	0.742	1.153	0.504	0.803
Langmuir	$q_{m,L}$	mmol U g^{-1}	0.822	1.231	0.598	0.878
	b_L	L $mmol^{-1}$	13.02	28.26	7.13	14.37
	R^2	–	0.992	0.939	0.977	0.977
	AIC	–	−62	−35	−59	−51
Freundlich	k_F	mmol U g^{-1}	0.841	1.404	0.550	0.915
	n_F	g $mmol^{-1}$	3.45	3.87	3.077	3.47
	R^2	–	0.947	0.907	0.913	0.939
	AIC	–	−45	−31	−47	−42
Sips	$q_{m,S}$	mmol U g^{-1}	0.810	1.340	0.513	0.887
	b_S	Unit	15.11	11.14	50.04	13.07
	n_S	–	0.958	1.289	0.562	1.027
	R^2	–	0.992	0.942	0.997	0.977
	AIC	–	−57	−31	−74	−46
Temkin	A_t	L $mmol^{-1}$	159.3	593.0	65.63	179.9
	b_T	J kg^{-1} mol^{-2}	15.41	12.12	18.97	14.58
	E_T	kJ mol^{-1}	20.78	10.51	37.65	18.16
	R^2	–	0.981	0.925	0.957	0.968
	AIC	–	−54	–33	−54	−48
D-R	q_{DR}	mmol U g^{-1}	0.804	1.254	0.563	0.865
	$k_{DR} \times 10^{11}$	mol^2 kJ^2	1.597	1.032	2.387	1.508
	E_{DR}	kJ mol^{-1}	7.91	9.84	6.47	8.14
	R^2	–	0.991	0.942	0.982	0.977
	AIC	–	−61	−36	−61	−51

value than the Langmuir equation (i.e., +6.8–18.7 %). The D-R sorption energy (E_{DR}, kJ mol^{-1}) ranges between 6.47 and 9.84 kJ mol^{-1}: generally, the sorption is systematically greater for BAP-based materials (*vs.* MAP-based sorbent) and for composite sorbents (beneficial effect of CuO incorporation). While considering the Langmuir equation (that is illustrated by the solid lines in Fig. 4), the same trends are observed for the affinity coefficient (b_L, L $mmol^{-1}$): the values are almost doubled between MAP- and BAP-based materials and after incorporation of CuO (hence, b_L(CuO-BAP) ≈ 4 b_L(MAP). The double aminophosphonation and the preparation of the composite material allow enhancing the sorbent affinity for UO_2^{2+} as well as the maximum sorption capacity.

Of course, the mechanistic Langmuir equation assumes a monolayer sorption to occur at the sorbent surface with similar sorption energies (sorbent homogeneity) and without interactions amongst the adsorbed molecules. However, here The incorporation of CuO NPs leads to the insertion of supplementary oxygen atoms, which may interact as supplementary reactive groups for U(VI) sorption. Therefore, different O-based functional groups coexist (brought by copper oxide and aminophosphonate moieties). These reactive groups have probably different binding energies for U(VI), contrary to the hypotheses for the application of the Langmuir equation. In this case, the Langmuir model can be extended to sorbents having surface heterogeneities. Herein, the Langmuir Dual Site (EDS) equation was tested unsuccessfully for fitting isotherm profiles. The mathematical fit of the experimental profiles means that the equation statistically models the data but with decorrelation to fundamental binding mechanisms.

Based on the relative fraction of the CuO in the composite sorbent and its contribution in the global sorption, this can be neglected in first approximation; though the synergism between polymer and CuO compartments cannot be rejected. It is also important reminding that the fact that the successful mathematical fit of experimental data by the Langmuir equation means necessarily that the mechanistic hypotheses of the model are fulfilled. These hypotheses must be theoretically verified at experimental level. The current case is probably a good example of the care to take into the physicochemical interpretation of mathematical fit of sorption isotherms. Here the Langmuir fit should be more considered as a comparison tool rather than a support for mechanism interpretation.

Also, with the evaluation of intrinsic sorption capacity of CuO and the relative proportion of CuO in the composite, we could demonstrate the specific contribution of the inorganic compartment and then probably the minimized effect of sorbent heterogeneity that make the Langmuir model to be more fitted.

Calculating the thermodynamic parameters (Fig. 4) is allowed by the sorption isotherms studying at a variety of temperatures (summarized in Table S9). Tran et al. [79] deeply discussed the van't Hoff equation rationale use in order to study the thermodynamics of sorption. They highlighted the necessity to use (a) a sufficient number of different temperatures (minimum: 4), (b) the affinity coefficient (or equivalent parameter for alternative equation) instead of the distribution ratio, and (c) the importance of using appropriate units (and dimension). This approach was selected herein for the calculation of thermodynamic variables (i.e., ΔS^0 entropy change, J mol^{-1} K^{-1}; ΔG^0 Gibbs free energy change, kJ mol-1 and ΔH^0 enthalpy change, kJ mol-1):

$$-\Delta G^0 = -RT\ln K_{eq}^0 = -RT\ln b_L \times \frac{C_{adsorbate}^0}{\gamma_{adsorbate}} \quad (1)$$

where $\gamma_{adsorbate}$ (≈ 1 for diluted solution) is the activity coefficient and $C_{adsorbate}^0$ (≈ 1 mol L^{-1}) is the adsorbate's unitary standard concentration, b_L should be in molar unit (i.e., L mol^{-1}).

$$\Delta G^0 = \Delta H^0 - T\Delta S^0 \quad (2)$$

$$\ln K_{eq}^0 = \frac{-\Delta H^0}{R} \times \frac{1}{T} + \frac{\Delta S^0}{R} \quad (3)$$

For the different sorbents, it is possible establishing the van't Hoff plots from Table S9, (Fig. S11). Table 3 summarizes the thermodynamic parameters. The enthalpy changes (ΔH^0) are systematically positive; this confirms the endothermic sorption of U(VI) onto the different materials. On the other hand, the increased randomness of the system after U(VI) sorption as indicated from the positive value of ΔS^0. Usually the negative ΔG^0 values are associated with spontaneous sorption. For MAP-based sorbents, the enthalpy change is not influenced by the incorporation of CuO; contrary to BAP-based sorbents, the enthalpy change decreases with the presence of CuO nanoparticles. This can elucidate the better affinity of this sorbent for uranyl ions; the lower enthalpy changes for BAP-based sorbents are also consistent with the better sorption performances of these sorbents compared with MAP-based materials. The randomness of the system increases greatly with MAP-based sorbents. It is noteworthy that the incorporation of CuO shows reciprocal trends for the two families of sorbents: decrease in randomness for BAP and increase for MAP.

Table S10 lists the sorption performances for different types of alternate sorbents. Since the experimental conditions are not identical (such as, pH, sorbent dosage, time and aqueous composition), a direct comparison is not easy. Overall, the maximum capacities were taken into consideration while comparing the various materials. Poly(amidoxime)/graphene oxide aerogel exhibits remarkable sorption characteristics for U(VI) that has high sorption capacity reaches to 2 mmol U g^{-1} at pH 4.5 [80]; compared to the sorption of CuO-BAP, this is approximately 70 % higher (although the affinity coefficient is lower

Table 3
Thermodynamic parameters for the sorption of U(VI) using selected sorbents.

T (°C)	BAP (R^2: 0.980)			CuO-BAP (R^2: 0.949)		
	ΔH°(kJ mol^{-1})	ΔS°(J mol^{-1} K^{-1})	ΔG°(kJ mol^{-1})	ΔH°(kJ mol^{-1})	ΔS°(J mol^{-1} K^{-1})	ΔG°(kJ mol^{-1})
25	32.09	74.4	−19.89	27.53	167.1	−22.25
35			−21.63			−23.92
45			−23.38			−25.59
55			−25.12			−27.26
T (°C)	MAP (R^2: 0.947)	CuO-MAP (R^2: 0.999)				
	ΔH°(kJ mol^{-1})	ΔS°(J mol^{-1} K^{-1})	ΔG°(kJ mol^{-1})	ΔH°(kJ mol^{-1})	ΔS°(J mol^{-1} K^{-1})	ΔG°(kJ mol^{-1})
25	38.17	187.5	−17.72	38.73	195.5	−19.53
35			−19.59			−21.49
45			−21.47			−2344
55			–23.34			−25.40

than for the current composite sorbent: 6.1 *vs.* 28.3 L mmol^{-1}). Another remarkable sorbent has been described by Ding et al. [81]: the sorption capacity of Al_2O_3-TiO_2 nanocomposite reaches 2.46 mmol U g^{-1} with a Langmuir affinity coefficient (b_L) as high as 578 L mmol^{-1}. While for picolylamine functionalized sorbent, Chen et al [82] stated also sorption capacity exceeding 2 mmol U g^{-1} (and a b_L value of 164 L mmol^{-1}) and a higher pH (i.e., pH 5.3). The composite sorbent shows sorption characteristics for U(VI) that are competitive with other candidates in terms of combined equilibrium and kinetic performances (at intermediary pH).

3.3.4. *Sorption mechanisms*

The functional groups accessible to metal sorption are –NH_2, >NH amine, (C=S), and (P=O) moieties, according to the suggested structure of the both materials presented in Scheme 1. Different uranium sorption modes (shown in Scheme 2) for the pristine sorbents (BAP and MAP) are suggested based on the analyses of materials before and after uranyl binding (FTIR, XPS, effect of pH, sorbent titration, etc.). The proposed different complexation mechanisms for metal sorption (via the multiple heteroatoms) are provided in detailed descriprion in (Section C, SI).

Raising the number of chelating rings improves the stability of the created complex, which improves metal sorption. As a result, the five-membered chelate rings produced by the contributing modes (I to III) are more stable than the four-membered rings produced by the contributing modes. Furthermore, an ion-exchange mechanism may take place through the –NH_2 groups (of the thiocarbazide molecule) that may be impacted by the Ph through uranyl speciation along with the protonation/deprotonation; the proposed anion-exchange mechanisms are not likely to occur: global ion-exchange reaction:

$$\left(R_2NH_2^+\right)_2SO_4^{2-} + UO_2(SO_4)_2^{2-} \leftrightarrow \left(R_2NH_2^+\right)_2UO_2(SO_4)_2^{2-} + SO_4^{2-} \quad (4a)$$

While an alternative mechanism can be postulated for the neutral sulfate sorption known as the molecular addition mechanism (Eq. (4b):

$$\left(R_2NH_2^+\right)_2SO_4^{2-} + UO_2SO_4 \leftrightarrow \left(R_2NH_2^+\right)_2UO_2(SO_4)_2^{2-} \quad (4b)$$

Uranium sorption onto CuO/BAP and CuO/MAP sorbents can be accomplished using.

two distinct procedures: the specified sorption by encapsulated copper oxide particles and the nonspecified sorption by the matrices material. In acidic conditions, the nonspecified uranyl sorption may take place through the protonated –CHO and –NH_2 moieties on the sorbent surface. While specified sorption may take place through the electrostatic attraction between the CuO sites (of the sorbent) and anionic uranyl species as well as the creation of inner-sphere complexes within oxidized copper sites [40]. Also, uranyl ions may be sorbed through coordination shell with OH groups as a result of the surface charges developed by the CuO surfaces subjected to water.

3.3.5. *Desorption and sorbent recycling*

Acid solutions are more frequently used [83,84] for uranium desorption from loaded sorbents in spite of the use of carbonate or bicarbonate solutions (due to the efficient complexation of uranyl with CO_3^{2-} and HCO_3^- [10,85,86]). Indeed, the treatment of the eluate for recovering uranium is made easier when the metal is free instead of being complexed. The investigation of the effect of the pH effect on U (VI) sorption for selected sorbents allows anticipating that metal binding can be reversed with working in acidic solutions. Hereafter, HCl (0.2 M) solution is selected to elute uranyl ions from BAP and MAP sorbents; on the other hand, for composite sorbents U(VI) elution is operated with an acidified 0.25 M urea solution (at pH 2.5). Acidic urea solutions were used to elute REEs from several functionalized sorbents [87]. Along six cycles of reuses, the efficiencies of sorption and desorption for the four sorbents are compared in Table 4. With recycling, the yields of sorption and desorption continuously diminish. However, the decreases are very limited; for example, at the ultimate cycle the loss in sorption varies between 6.3 % and 7.0 % (compared with the performance at the first

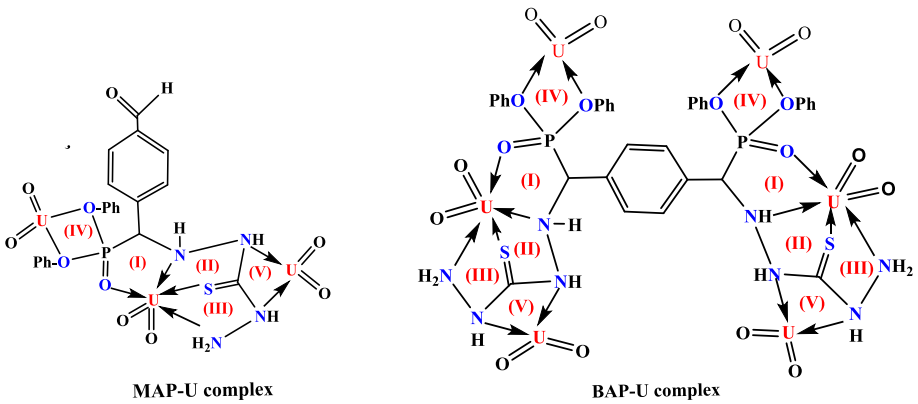

Scheme 2. Tentative mechanisms for the complexation of U(VI) with specific functional groups on BAP and MAP sorbents.

Table 4
Sorption and desorption at sorbent recycling.

Sorbent	BAP				CuO/BAP			
Operation	SE (%)		DE (%)		SE (%)		DE (%)	
Cycle	Aver.	St.Dev.	Aver.	St.Dev.	Aver.	St.Dev.	Aver.	St.Dev.
1	100.00	0.00	98.19	0.26	100.00	0.00	98.17	0.19
2	97.63	0.03	97.81	0.08	97.88	0.09	97.91	0.67
3	95.99	0.02	96.78	0.27	96.48	0.16	96.89	0.54
4	95.27	0.06	95.51	0.07	95.49	0.04	95.89	0.30
5	94.23	0.08	94.47	0.05	94.78	0.18	94.94	0.22
6	93.19	0.04	93.28	0.17	93.73	0.28	93.99	0.44
Loss at 6th (%)	−6.81		−4.91		−6.27		−4.18	
Sorbent	MAP				CuO/MAP			
Operation	SE (%)		DE (%)		SE (%)		DE (%)	
Cycle	Aver.	St.Dev.	Aver.	St.Dev.	Aver.	St.Dev.	Aver.	St.Dev.
1	100.00	0.00	98.16	0.20	100.00	0.00	98.37	0.25
2	97.46	0.11	97.42	0.61	97.63	0.12	97.61	0.31
3	96.35	0.10	96.28	0.29	96.30	0.19	96.43	0.35
4	94.99	0.08	95.35	0.28	95.37	0.23	95.65	0.12
5	93.69	0.56	94.57	0.10	94.25	0.11	94.70	0.16
6	92.99	0.31	93.40	0.01	93.21	0.10	93.91	0.01
Loss at 6th (%)	−7.01		−4.76		−6.79		−4.46	

Variations in sorption and desorption performances are individually “normalized” with reference values at the first step.

cycle) and between 4.2 % and 4.9 % in terms of desorption. The incomplete desorption (which decreases the reactive groups density accessible to U(VI) sorption) as well as the sorbents degradation may explain the reduction in sorption efficiency. This degradation of the sorbents that marginally depreciate uranyl sorption was illustrated by the modifications of the sorbents, both in terms of organic fraction (FTIR characterizations) but also concerning the CuO compartment (Cu 4*f* XPS changes observed after U(VI) sorption).

Notably, the losses in sorption and desorption are limited and almost equivalent for the different sorbents. This property makes the sorbent promising for uranium recovery from dilute solutions (and mild acid conditions), although larger number of recycling steps would be necessary for evaluating the effective commercial potential. Yuan et al. [88] observed a 9.5 % decrease in uranyl sorption by phosphonic acid functionalized polymer at the seventh recycling. Significantly, the phosphonation of cellulose supports not only increased the sorption of uranyl but also the stability of the sorbents at recycling [89]. In the case of CMC/Ca-rectorite composite, the loss in U(VI) sorption did not exceed 5 % [90]. Li et al. [91] reports the greater stability at recycling of metal–organic framework for UO_2^{2+} (99 % to 94 %) compared with ReO_4^- (40 % to 32 %). Another important criterion for evaluating this feasibility consists of testing the sorption properties in complex solutions and evaluating the selectivity of the sorbents for target uranyl ions. The chemical stability of the CuO nanocomposites was studied for and testing the stability of organic polymer exposed to acidic (or alkaline) reagent (see Section D in SI). Additionally, after the nanocomposites were treated with HCl solution (0.2 M, pH: 1.03) and FTIR analysis for the samples was carried out (as shown in the in **Fig. S12**). After treatment, the mass loss was determined and found to be ~4.9–6.9 %.

3.4. Egyptian ore application to U recovery

3.4.1. Ore leachate – Metal extraction and pre-treatment

The ore composition (including major and trace components) is reported in Table S11. Based on geological characteristics of the mining area (see Section E in SI) and the mineral nature of the ore (aluminosilicate), the major elements (present as oxides) are silicon and aluminum (about 51.6 %). Iron oxide is also an important constituent (about 11.1 %) while oxides of alkali and alkali-earth elements represent 18.7 %. It is also noticeable that the ore contains significant amounts of sulfate (≈2.8 %), chloride (≈2.4 %), and phosphate (≈1 %). The loss on ignition counts for 11 %; meaning that organic substances and carbonate represent a significant fraction of the ore. Apart these major elements, trace elements such as titanium and manganese (up to ≈1.3 %) are also present; the presence of MnO_2 is of great interest for uranium leaching. Indeed, uranium (with content close to 270 mg kg^{-1}) is present in primary mineral source (as U(VI)) but also as secondary mineral state (as U (IV)). In acidic solution manganese oxide will contribute to the oxidation of U(IV) for enhancing the leaching of the metal (which reaches 89 % in the pregnant liquor solution, PLS; at concentration ≈240 mg L^{-1}). The leaching extracted huge amounts of silicon, aluminum (at concentrations up to 52.7 and 39.9 g L^{-1}, respectively). Sodium and potassium are almost fully dissolved (>97 %) with concentrations counting for 5.7 and 9.4 g L^{-1}, respectively. For alkali-earth elements, the leaching yields 12.4–18.6 % (with concentrations 10.7–7.5 g L^{-1}, respectively). Iron is also present at high concentration in the leachate (up to 6.7 g L^{-1}, leaching efficiency: 6 %); this presence is critical for the sorption process. Indeed, the necessity to increase the pH (up to 4–4.5) for optimization of uranyl sorption by selected sorbents causes the precipitation of the metal (and the accompanying precipitation of additional metal ions). The composition of the pre-treated PLS (pH-adjusted PLS, PPLS) is also reported in Table S11, with calculation of metal precipitation. It is noteworthy that the pre-treatment of PLS does not significantly affect uranium concentration (loss does not exceed 6 %), contrary to iron (61.6 %). The precipitation of other metals varies from (31.2 % (for Al(III) to 7 % (for Mg(II). In any cases, the residual concentrations in the filtrated PPLS solution reach huge values for competitor ions such as Si(IV) and Al(III) with molar excess compared with U(VI) up to 1458-fold and 1071-fold, respectively. The alkali and alkali-earth metal ions are also in large excess (from 214-fold to 301-fold). Though at lower concentrations, other competitor ions such as Ti(IV), Fe(III), P(V), and Mn(II) are in excess compared with U(VI) by31-fold to 85-fold. Actually, despite the precipitation step, the composition of PPLS remains complex and offers a good opportunity for assaying the potential of the sorbents for uranium recovery and for evaluating their selectivity in real conditions.

3.4.2. Uranium sorption and selective separation

The sorption capacities of the sorbents for selected metal (or elements) are compared in Fig. 5 (at pH 4.5). First, it appears that the sorbents have a broad reactivity for the different elements. This is confirmed by the EDX analysis of the sorbents surface after PPLS contact (Table S12). Apart the proper reactivity of CuO nanoparticles, the existence of primary and secondary amine groups (intermediary base character), phosphonate moieties (hard base), and sulfide (soft base) may implies the good affinity of the multifunctional sorbents for a broad family of metals according Pearson’s principles [20]. Though most of the

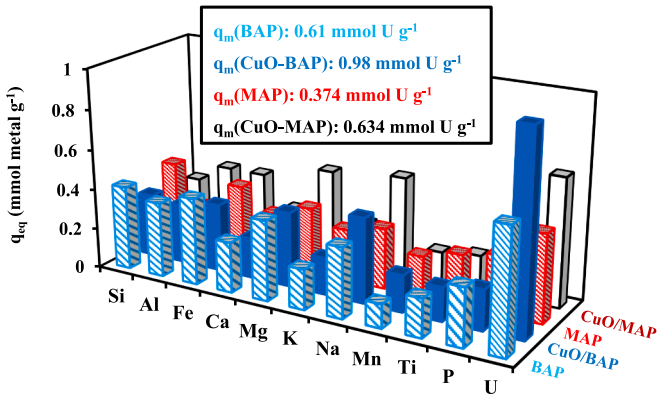

Fig. 5. Treatment of PPLS by sorption onto selected sorbents – Sorption capacities of selected elements (pH_0: 4.5, SD: 0.5 g L^{-1}; time: 60 min; T: 25 ± 1 °C; v: 200 rpm).

elements investigated are part of hard metals, some of these metals are at the frontier (or belong to) of the intermediary domain according to Nieboer and Richardson [92]. The diversity of functional groups opens the route for wider reactivity for metals of different configurations. However, there are some remarkable findings to highlight:

(a) The higher sorption capacities reached for U(VI) (despite much lower metal concentration);
(b) The ranking in U sorption capacity according to CuO-BAP≫CuO-MAP ≈ BAP≫MAP;
(c) The CuO-BAP composite exhibits, in general, a lower affinity for metal ions (other than U(VI), Na(I), Mn(II)) compared with BAP;
(d) The cumulative sorption capacities (mmol g^{-1}) are comparable for the different sorbents: CuO-BAP(3.65) ≈ CuO-MAP(3.64) ≈ BAP(3.61) > MAP(3.32).

It is noteworthy that elements, uranium sorption capacities are close to maximum sorption capacities attained using synthetic solutions regardless of the massive excess of competing elements. The sorption capacity loss varies between 14 % and 21 %. The much higher cumulative sorption capacity (3.32–3.65 mmol g^{-1}) also means that the competitor elements are bound through alternative reactive groups or mechanisms in Fig. S13a.

The distribution ratios (D L g^{-1}) are compared which clearly highlights the singular concentration effect of the materials for uranyl ions compared to the other elements (in huge excess in solution). Consistently with the conclusions raised with synthetic solutions, the D values are ranked according to: CuO-BAP(2.145) ≫ CuO-MAP(1.002) ≈ BAP (0.94) ≫ MAP(0.591). The contributions of the CuO nano-particles and the bis-phosphonation allow designing sorbent with increasing concentration effect and higher selectivity (Fig. S13b) for U(VI). The selectivity coefficient $SC_{Metal/Fe}$ is defined as:

$$SC_{Metal/Fe} = \frac{D_{metal}}{D_{Fe}} = \frac{q_{eq,Metal} \times C_{eq,Fe}}{C_{eq,Metal} \times q_{eq,Fe}} \quad (5)$$

Iron was selected for the reference because Fe(III) shows the highest distribution ratio among the other competitor elements. Within the current experimental conditions, this indicates that the sorbents have lower preference for other elements than Fe(III) (independently of their relative concentrations in PPLS); with the remarkable exception of uranyl. Regardless the massive excess of these competing elements, the sorbents exhibit strong uranyl selectivity for U(VI) ($SC_{U/metal}$) compared with different solutes, according the series:

CuO-BAP(>293)≫CuO-MAP(>123) > Bap(>100) > MAP(>73)

As a conclusion, in complex solution the sorbents have a marked preference for uranyl although they can bind all the elements at different extents. The sorbent type has a weak effect on the maximum sorption capacity. Apparently, the other metal ions are bound through different mechanisms and functional groups, because of the limited impact on uranyl sorption.

3.4.3. *Yellow cake production*

In order to evaluate the potential for uranium valorization, the saturated sorbents were investigated for desorption with HCl (0.2 M) solution (for aminophosphonate matrices) and 0.25 M urea (at pH 2.5). Uranium desorption reaches 90 %, 92 %, 88 % and 91 % for BAP, CuO/BAP, MAP and CuO/MAP, respectively. As sown in Table 4, this is slightly less than for sorbents loaded with single-component uranyl solutions. This slight decrease can be explained by existence of another elements loaded upon the sorbent. U(VI) elution can be enhanced by alteration the acid concentration or the solid/liquid ratio.

In order to recover uranium, the eluates were treated by precipitation with ammonium hydroxide (25 % w/w solution), and controlling the pH to 7.5. Ammonium diuranate (yellow precipitate) is collected by filtration, dried at 110 °C for 2 h. The EDX analysis of the yellow cakes is reported in Table S13. The higher selectivity of the CuO sorbents allows reaching higher grade than the pristine sorbents. The final product obtained after precipitation contains substantial impurities: about 15 % (constituted of Fe, Ca, S, Mg and Si) and 22.3 % (constituted of Cu, K, Ca, S, Mg and Si) in the case of eluates produced from CuO/BAP and CuO/MAP, respectively. The U content approaches 85.1 % and 77.7 % (in weight) for CuO/BAP and CuO/MAP, respectively. For BAP and MAP, uranium represents 76.6 % and 68 %, respectively; the impurities in eluates reach about 23.4 % (constituted of (Fe and K) around 6.41 %, and (Mg, Al and Si) at about 16.8 %) for BAP, and 32.0 % (constituted of (Fe and S) around 14.3 %, and (Mg, Al and Si) at about 17.9 %) for MAP.

It is noteworthy that iron represents up to 9.44 % (in weight) of the yellow cake produced from MAP, in addition to the existence of another metals and elements in substantial amounts; these amounts are higher than what is considered acceptable for yellow cake on the market.. A complementary purification step will be necessary for reaching commercial grade criteria.

4. Conclusions

Two aminophosphonate matrices (BAP and MAP) are synthesized through the simple reaction of trimethylphosphite, thiocarbazide and p-phthalaldehyde with different molar ratios). In a second step, two CuO/ nanocomposites are *in situ* generated by impregnation of the aminophosphonate matrices with Cu(II) (as aqueous copper sulfate solution), followed by internal and surface precipitation (with sodium hydroxide), at room temperature. The synthesis conditions (leading to bis- *vs.* monophosphonation) affect the textural properties and the deprotonation properties, with implications on U(VI) sorption.

Uptake kinetics can be fitted by (PSORE), while the sorption isotherms are modeled by the Langmuir model as well as the Dubinin-Raduskevich equation. The CuO NPs incorporation increases the maximum sorption capacity of the pristine sorbents by ~56.76 % (from 0.74 to 1.16 mmol U g^{-1}) from BAP to CuO/BAP and by ~60 % (from 0.5 to 0.8 mmol U g^{-1}) from MAP to CuO/MAP at pH_0 4.5 and T: 25 ± 1 °C. This enhancement is correlated to increased specific surface area (for higher accessibility and availability of binding sites, for composite materials), and to the increase in functional groups (for BAP- *vs.* MAP-based sorbents). The U(VI) sorption is endothermic and spontaneous with increased randomness as shown by the thermodynamic parameters. The sorbents are highly stable with little decrease in sorption and desorption performances (lower than 7 % and lower than 5 %, respectively) when reused for 6 successive cycles; using 0.2 M HCl for BAP and MAP, and 0.25 M acidified urea (pH 2.5) as eluents.

CuO-based nanocomposites show substantially higher selectivity for uranyl ions than the pristine materials through the treating of Egyptian

ore acidic leachate that have significant excesses of alkali and alkaline-earth elements (along with other major components such as iron and silica). By the comparison with of single-component uranyl synthetic solutions, the sorption capacities for BAP, CuO/BAP, MAP and CuO/MAP are only decreased by 18.4 %, 15.0 %, 13.8 % and 21.2 % respectively, regardless the massive excess of accompanied elements,

The overall sorption capacities reach significant levels (i.e., 3.61, 3.65, 3.32 and 3.64 mmol g^{-1}, respectively); this indicates that the potential sorption of another elements, which is promoted by high concentrations, slightly restricts the uranyl sorption and that the sorption of such elements may include other functional groups. Nevertheless, metal after being eluted from the sorbent and precipitated by amm.hydroxide, the large concentrations of such co-elements prevent the production of high-purity yellow cakes.

As a conclusion, CuO-BAP reveals an interesting, extremely effective, reused, and economic nano-sorbents for the effectively recovery of U (VI), even in complex industrial effluent.

CRediT authorship contribution statement

Enas A. Imam: Conceptualization, Methodology, Investigation, Validation, Writing – original draft. **Ahmed I. Hashem:** Conceptualization, Methodology, Investigation, Writing – review & editing. **Ahmad A. Tolba:** Conceptualization, Methodology, Investigation, Writing – review & editing. **Mohammad G. Mahfouz:** Conceptualization, Methodology, Investigation, Writing – review & editing. **Ibrahim El-Tantawy El-Sayed:** Conceptualization, Methodology, Investigation, Writing – review & editing. **Hamada B. Hawash:** Conceptualization, Methodology, Investigation, Writing – review & editing. **Rana R. Neiber:** Formal analysis, Data curation, Writing – original draft. **Hamed I. Mira:** . **Ahmed A. Galhoum:** Conceptualization, Methodology, Investigation, Writing – review & editing. **Eric Guibal:** Conceptualization, Software, Formal analysis, Data curation, Writing – review & editing.

Declaration of Competing Interest

The authors declare that they have no known competing financial interests or personal relationships that could have appeared to influence the work reported in this paper.

Data availability

Data will be made available on request.

Acknowledgements

Authors acknowledge Nuclear Materials Authority (Egypt) for their support. Special dedication to the memory of Prof. Ahmed Donia.

Appendix A. Supplementary material

Supplementary data to this article can be found online at https://doi.org/10.1016/j.seppur.2023.124466.

References

[1] C.-R. Zhang, W.-R. Cui, C.-P. Niu, S.-M. Yi, R.-P. Liang, J.-X. Qi, X.-J. Chen, W. Jiang, L. Zhang, J.-D. Qiu, rGO-based covalent organic framework hydrogel for synergistically enhance uranium capture capacity through photothermal desalination, Chem. Eng. J. 428 (2022), 131178.
[2] D. Wang, J. Song, S. Lin, J. Wen, C. Ma, Y. Yuan, M. Lei, X. Wang, N. Wang, H. Wu, A marine-inspired hybrid sponge for highly efficient uranium extraction from seawater, Adv. Funct. Mater. 29 (2019) 1901009.
[3] B. Yan, C. Ma, J. Gao, Y. Yuan, N. Wang, An ion-crosslinked supramolecular hydrogel for ultrahigh and fast uranium recovery from seawater, Adv. Mater. 32 (2020) 1906615.
[4] Y. Yuan, S. Feng, L. Feng, Q. Yu, T. Liu, N. Wang, A bio-inspired nano-pocket spatial structure for targeting uranyl capture, Angew. Chem. Int. Ed. 59 (2020) 4262–4268.
[5] S. Shi, Y. Qian, P. Mei, Y. Yuan, N. Jia, M. Dong, J. Fan, Z. Guo, N. Wang, Robust flexible poly(amidoxime) porous network membranes for highly efficient uranium extraction from seawater, Nano Energy 71 (2020), 104629.
[6] M. Ahmad, J. Chen, K. Yang, T. Shah, M.-u.-d. Naik, Q. Zhang, B. Zhang, Preparation of amidoxime modified porous organic polymer flowers for selective uranium recovery from seawater, Chem. Eng. J. 418 (2021), 129370.
[7] H. Zhang, W. Liu, A. Li, D. Zhang, X. Li, F. Zhai, L. Chen, L. Chen, Y. Wang, S. Wang, Three bechanisms in one material: uranium capture by a polyoxometalate–organic framework through combined complexation, chemical reduction, and photocatalytic reduction, Angew. Chem. Int. Ed. 58 (2019) 16110–16114.
[8] X. Liu, J. Li, X. Wang, C. Chen, X. Wang, High performance of phosphate-functionalized graphene oxide for the selective adsorption of U(VI) from acidic solution, J. Nucl. Mater. 466 (2015) 56–64.
[9] C. Yawen, W. Chunfang, Z. Liu, L. Zhang, L. Chen, J.-Q. Wang, X. Wang, S. Yang, S. Wang, Fabrication of phosphorylated graphene oxide-chitosan composite for highly effective and selective capture of U(VI), Environ. Sci.: Nano 4 (2017).
[10] E.A. Imam, I. El-Tantawy El-Sayed, M.G. Mahfouz, A.A. Tolba, T. Akashi, A. A. Galhoum, E. Guibal, Synthesis of α-aminophosphonate functionalized chitosan sorbents: Effect of methyl vs phenyl group on uranium sorption, Chem. Eng. J. 352 (2018) 1022–1034.
[11] Y. Xie, C. Chen, X. Ren, X. Wang, H. Wang, X. Wang, Emerging natural and tailored materials for uranium-contaminated water treatment and environmental remediation, Prog. Mater Sci. 103 (2019) 180–234.
[12] Z. Huang, H. Dong, N. Yang, H. Li, N. He, X. Lu, J. Wen, X. Wang, Bifunctional phosphorylcholine-modified adsorbent with enhanced selectivity and antibacterial property for recovering uranium from seawater, ACS Appl. Mater. Interfaces 12 (2020) 16959–16968.
[13] A.A. Galhoum, Mesoporous chitosan derivatives for effective uranyl sorption: synthesis, characterization, and mechanism-application to ore leachate, Int. J. Biol. Macromol. 242 (2023), 124634.
[14] M.K. Sureshkumar, D. Das, M.B. Mallia, P.C. Gupta, Adsorption of uranium from aqueous solution using chitosan-tripolyphosphate (CTPP) beads, J. Hazard. Mater. 184 (2010) 65–72.
[15] L.-Y. Yuan, Y.-L. Liu, W.-Q. Shi, Y.-L. Lv, J.-H. Lan, Y.-L. Zhao, Z.-F. Chai, High performance of phosphonate-functionalized mesoporous silica for U(VI) sorption from aqueous solution, Dalton Trans. 40 (2011) 7446–7453.
[16] S.S. Lee, W. Li, C. Kim, M. Cho, J.G. Catalano, B.J. Lafferty, P. Decuzzi, J. D. Fortner, Engineered manganese oxide nanocrystals for enhanced uranyl sorption and separation, Environ. Sci. Nano 2 (2015) 500–508.
[17] Z. Wang, C. Xu, Y. Lu, F. Wu, G. Ye, G. Wei, T. Sun, J. Chen, Visualization of adsorption: luminescent mesoporous silica-carbon dots composite for rapid and selective removal of U(VI) and in situ monitoring the adsorption behavior, ACS Appl. Mater. Interfaces 9 (2017) 7392–7398.
[18] M. Zhao, Z. Cui, D. Pan, F. Fan, J. Tang, Y. Hu, Y. Xu, P. Zhang, P. Li, X.-Y. Kong, W. Wu, An efficient uranium adsorption magnetic platform based on amidoxime-functionalized flower-like Fe_3O_4@TiO_2 core–shell microspheres, ACS Appl. Mater. Interfaces 13 (2021) 17931–17939.
[19] M.M. Rashad, I.E. El-Sayed, A.A. Galhoum, M.M. Abdeen, H.I. Mira, E.A. Elshehy, S. Zhang, X. Lu, J. Xin, E. Guibal, Synthesis of α-aminophosphonate based sorbents – influence of inserted groups (carboxylic vs. amine) on uranyl sorption, Chem. Eng. J. 421 (2021), 127830.
[20] R.G. Pearson, Hard and soft acids and bases, J. Am. Chem. Soc. 85 (1963) 3533–3539.
[21] A. Amira, Z. Aouf, H. K'tir, Y. Chemam, R. Ghodbane, R. Zerrouki, N.-E. Aouf, Recent advances in the synthesis of α-aminophosphonates: a review, ChemistrySelect 6 (2021) 6137–6149.
[22] D.A. Elsherbiny, A.M. Abdelgawad, M.E. El-Naggar, R.A. El-Sherbiny, M.H. El-Rafie, I.-E.-T. El-Sayed, Synthesis, antimicrobial activity, and sustainable release of novel α-aminophosphonate derivatives loaded carrageenan cryogel, Int. J. Biol. Macromol. 163 (2020) 96–107.
[23] R.R. Neiber, A.A. Galhoum, I. El-Tantawy El Sayed, E. Guibal, J. Xin, X. Lu, Selective lead (II) sorption using aminophosphonate-based sorbents: effect of amine linker, characterization and sorption performance, Chem. Eng. J. 442 (2022), 136300.
[24] H. Fernández-Pérez, P. Etayo, A. Panossian, A. Vidal-Ferran, Phosphine−phosphinite and phosphine−phosphite ligands: preparation and applications in asymmetric catalysis, Chem. Rev. 111 (2011) 2119–2176.
[25] W. Tang, X. Zhang, New chiral phosphorus ligands for enantioselective hydrogenation, Chem. Rev. 103 (2003) 3029–3070.
[26] Y. Ren, R. Yang, L. Shao, H. Tang, S. Wang, J. Zhao, J. Zhong, C. Kong, The removal of aqueous uranium by SBA-15 modified with phosphoramide: a combined experimental and DFT study, RSC Adv. 6 (2016) 68695–68704.
[27] V.P. Kukhar, V.D. Romanenko, Chemistry of aminophosphonic acids and phosphonopeptides, in: Amino Acids, Peptides and Proteins in Organic Chemistry, Wiley-VCH Verlag GmbH & C, KGaA, Weinheim (Germany), 2009, pp. 189–260.
[28] S.D. Alexandratos, X. Zhu, M. Florent, R. Sellin, Polymer-supported bifunctional amidoximes for the sorption of uranium from seawater, Ind. Eng. Chem. Res. 55 (2016) 4208–4216.
[29] J. Muller, B. Prelot, J. Zajac, S. Monge, Synthesis and study of sorption properties of polyvinyl alcohol (PVA)-based hybrid materials, React. Funct. Polym. 144 (2019), 104364.

[30] Y. Zhou, Y. Gao, H. Wang, M. Xia, Q. Yue, Z. Xue, J. Zhu, J. Yu, W. Yin, Versatile 3D reduced graphene oxide/poly(amino-phosphonic acid) aerogel derived from waste acrylic fibers as an efficient adsorbent for water purification, Sci. Total Environ. 776 (2021), 145973.

[31] S. Zhu, M. Xia, Y. Chu, M.A. Khan, W. Lei, F. Wang, T. Muhmood, A. Wang, Adsorption and desorption of Pb(II) on l-lysine modified montmorillonite and the simulation of interlayer structure, Appl. Clay Sci. 169 (2019) 40–47.

[32] E.A. Imam, A.I. Hashem, A.A. Tolba, M.G. Mahfouz, I.-E.-T. El-Sayed, A.I. El-Tantawy, A.A. Galhoum, E. Guibal, Effect of mono- vs. bi-functionality of aminophosphonate derivatives on the enhancement of U(VI) sorption: physicochemical properties and sorption performance, J. Environ Chem. Eng. 11 (2023), 109951.

[33] D. Gomes Rodrigues, S. Monge, S. Pellet-Rostaing, N. Dacheux, D. Bouyer, C. Faur, Sorption properties of carbamoylmethylphosphonated-based polymer combining both sorption and thermosensitive properties: New valuable hydrosoluble materials for rare earth elements sorption, Chem. Eng. J. 355 (2019) 871–880.

[34] S.D. Alexandratos, X. Zhu, Polymer-supported aminomethylphosphinate as a ligand with a high affinity for U(VI) from phosphoric acid solutions: combining variables to optimize ligand–ion communication, Solvent Extr. Ion Exch. 34 (2016) 290–295.

[35] S.D. Alexandratos, X. Zhu, The Effect of hydrogen bonding in enhancing the ionic affinities of immobilized monoprotic phosphate ligands, Materials 10 (2017).

[36] X. Zhu, S.D. Alexandratos, Development of a new ion-exchange/coordinating phosphate ligand for the sorption of U(VI) and trivalent ions from phosphoric acid solutions, Chem. Eng. Sci. 127 (2015) 126–132.

[37] S. Sundar G. Venkatachalam S.J. Kwon Biosynthesis of copper oxide (CuO) nanowires and their use for the electrochemical sensing of dopamine 2018 Nanomaterials (Basel, Switzerland) 8.

[38] J. Zhu, H. Bi, Y. Wang, X. Wang, X. Yang, L. Lu, Synthesis of flower-like CuO nanostructures via a simple hydrolysis route, Mater. Lett. 61 (2007) 5236–5238.

[39] A. Goswami, P.K. Raul, M.K. Purkait, Arsenic adsorption using copper (II) oxide nanoparticles, Chem. Eng. Res. Des. 90 (2012) 1387–1396.

[40] K.Z. Elwakeel, E. Guibal, Arsenic(V) sorption using chitosan/$Cu(OH)_2$ and chitosan/CuO composite sorbents, Carbohydr. Polym. 134 (2015) 190–204.

[41] S. Archana, K.Y. Kumar, S. Olivera, B.K. Jayanna, H.B. Muralidhara, A. Ananda, C. C. Vidyasagar, Development of multipurpose CuO–GO nanocomposites for heavy metals adsorption and super capacitor applications, Energy Environ. 5 (2016) 305–315.

[42] P.K. Raul, S. Senapati, A.K. Sahoo, I.M. Umlong, R.R. Devi, A.J. Thakur, V. Veer, CuO nanorods: a potential and efficient adsorbent in water purification, RSC Advances 4 (2014) 40580–40587.

[43] A.A. Elzoghby, A. Bakry, A.M. Masoud, W.S. Mohamed, M.H. Taha, T.F. Hassanein, Synthesis of polyamide-based nanocomposites using green-synthesized chromium and copper oxides nanoparticles for the sorption of uranium from aqueous solution, J. Environ. Chem. Eng. 9 (2021), 106755.

[44] M. Bordbar, Z. Sharifi-Zarchi, B. Khodadadi, Green synthesis of copper oxide nanoparticles/clinoptilolite using Rheum palmatum L. root extract: high catalytic activity for reduction of 4-nitro phenol, rhodamine B, and methylene blue, J. Sol-Gel Sci. Technol. 81 (2017) 724–733.

[45] M. Naushad, T. Ahamad, G. Sharma, A.a.H. Al-Muhtaseb, A.B. Albadarin, M. M. Alam, Z.A. Alothman, S.M. Alshehri, A.A. Ghfa, Synthesis and characterization of a new starch/SnO_2 nanocomposite for efficient adsorption of toxic Hg^{2+} metal ion, Chem. Eng. J. 300 (2016) 306–316.

[46] X. Hou, A. Mensah, M. Zhao, Y. Cai, Q. Wei, Facile controlled synthesis of monodispersed MoO_3-MoS_2 hybrid nanospheres for efficient hydrogen evolution reaction, Appl. Surf. Sci. 529 (2020), 147115.

[47] A.A. Al-Ghamdi, A.A. Galhoum, A. Alshahrie, Y.A. Al-Turki, A.M. Al-Amri, S. Wageh, Mesoporous magnetic cysteine functionalized chitosan nanocomposite for selective Uranyl ions sorption: experimental, structural characterization, and mechanistic studies, Polymers 14 (2022).

[48] A.F. Abdel-Magied, H.N. Abdelhamid, R.M. Ashour, X. Zou, K. Forsberg, Hierarchical porous zeolitic imidazolate frameworks nanoparticles for efficient adsorption of rare-earth elements, Micropor. Mesopor. Mater. 278 (2019) 175–184.

[49] P.G. Bhavyasree, T.S. Xavier, Green synthesis of copper oxide/carbon nanocomposites using the leaf extract of adhatoda vasica nees, their characterization and antimicrobial activity, Heliyon 6 (2020) e03323.

[50] Sirajuddin, A. Mechler, A.A.J. Torriero, A. Nafady, C.-Y. Lee, A.M. Bond, A. P. O'Mullane, S.K. Bhargava, The formation of gold nanoparticles using hydroquinone as a reducing agent through a localized pH change upon addition of NaOH to a solution of $HAuCl_4$, Colloids Surf. A 370 (2010) 35–41.

[51] M. Singh, I. Sinha, R.K. Mandal, Role of pH in the green synthesis of silver nanoparticles, Mater. Lett. 63 (2009) 425–427.

[52] N.K. Farhana, F.S. Omar, N. Mohamad Saidi, G.Z. Ling, S. Bashir, R. Subramaniam, R. Kasi, J. Iqbal, S. Wageh, H. Algarni, A.G. Al-Sehemi, Modification of DSSC based on polymer composite gel electrolyte with copper oxide nanochain by shape effect, Polymers 14 (2022) 3426.

[53] Y.X. Zhang, M. Huang, F. Li, Z.Q. Wen, Controlled synthesis of hierarchical CuO nanostructures for electrochemical capacitor electrodes, Int. J. Electrochem. Sci. 8 (2013) 8645–8661.

[54] M. Thommes, K. Kaneko, A.V. Neimark, J.P. Olivier, F. Rodriguez-Reinoso, J. Rouquerol, K.S.W. Sing, Physisorption of gases, with special reference to the evaluation of surface area and pore size distribution (IUPAC Technical Report), Pure Appl. Chem. 87 (2015) 1051–1069.

[55] A. Popa, R. Ene, D. Visinescu, E.S. Dragan, G. Ilia, S. Iliescu, V. Parvulescu, Transitional metals immobilized by coordination on aminophosphonate functionalized copolymers and their catalytic properties, J. Mol. Catal. A: Chem. 408 (2015) 262–270.

[56] L.-F. Wu, Y.-H. Wang, P.-L. Li, X. Wu, M. Shang, Z.-Z. Xiong, H.-J. Zhang, F. Liang, Y.-F. Xie, J. Wang, Enhanced nonlinear optical behavior of graphene-CuO nanocomposites investigated by Z-scan technique, J. Alloys Compd. 777 (2019) 759–766.

[57] G.N.S. Vijayakumar, S. Devashankar, M. Rathnakumari, P. Sureshkumar, Synthesis of electrospun ZnO/CuO nanocomposite fibers and their dielectric and non-linear optic studies, J. Alloys Compd. 507 (2010) 225–229.

[58] S. Das, V.C. Srivastava, Synthesis and characterization of ZnO/CuO nanocomposite by electrochemical method, Mater. Sci. Semicond. Process. 57 (2017) 173–177.

[59] S. Omwoma Lugasi, New synthetic pathways for thiocarbohydrazide and salicylaldehyde azine compounds, Asian, J. Chem. Sci. 3 (2017) 1–8.

[60] A.S. Morshedy A.A. Galhoum A. Aleem H. Abdel Aleem M.T. Shehab El-din D.M. Okaba M.S. Mostafa H.I. Mira Z. Yang I.-E.-T. El-Sayed Functionalized aminophosphonate chitosan-magnetic nanocomposites for Cd(II) removal from aqueous solutions: Performance and mechanisms of sorption Appl. Surf. Sci. 561 (2021) 150069.

[61] S.H. Kismat Ara Elachi, M.M. Haque, Ranjan K. Mohapatra, Kudrat-E-Zahan, Synthesis, spectral and thermal characterization of Cu(II) complexes containing schiff base ligands and their antibacterial activity study, Am. J. Mater. Synth. Process. 4 (2019) 43–53.

[62] M.C. Zenobi, C.V. Luengo, M.J. Avena, E.H. Rueda, An ATR-FTIR study of different phosphonic acids in aqueous solution, Spectrochim. Acta, Part A 70 (2008) 270–276.

[63] D. Shao, G. Hou, J. Li, T. Wen, X. Ren, X. Wang, PANI/GO as a super adsorbent for the selective adsorption of uranium(VI), Chem. Eng. J. 255 (2014) 604–612.

[64] M.J. Manos, M.G. Kanatzidis, Layered metal sulfides capture uranium from seawater, J. Am. Chem. Soc. 134 (2012) 16441–16446.

[65] V. Dhanya, B. Arunraj, N. Rajesh, Prospective application of phosphorylated carbon nanofibers with a high adsorption capacity for the sequestration of uranium from ground water, RSC Adv. 12 (2022) 13511–13522.

[66] Z. Huang, Z. Li, L. Zheng, L. Zhou, Z. Chai, X. Wang, W. Shi, Interaction mechanism of uranium(VI) with three-dimensional graphene oxide-chitosan composite: Insights from batch experiments, IR, XPS, and EXAFS spectroscopy, Chem. Eng. J. 328 (2017) 1066–1074.

[67] S. Sunder, J.J. Cramer, N.H. Miller, Geochemistry of the Cigar Lake uranium deposit: XPS studies, Radiochim. Acta 74 (1996) 303–308.

[68] R. Williams, pKa data (compiled by R. Williams), in: O.D. AcCS (Ed.), University of Wisconsin, Chemistry Department, 2022.

[69] A.A. Galhoum, W.H. Eisa, I.-E.-T. El-Sayed, A.A. Tolba, Z.M. Shalaby, S. I. Mohamady, S.S. Muhammad, S.S. Hussien, T. Akashi, E. Guibal, A new route for manufacturing poly(aminophosphonic)-functionalized poly(glycidyl methacrylate)-magnetic nanocomposite - application to uranium sorption from ore leachate, Environ. Pollut. 264 (2020), 114797.

[70] S.A.M.A. Hubbe, S. Douven, Implications of apparent pseudo-second-order adsorption kinetics onto cellulosic materials: a review, BioRes. 14 (2019) 7582–7626.

[71] Y. Marcus, Ion Properties, Marcel Dekker Inc, New York, NY, 1997.

[72] K.A. Venkatesan, D.K. Patre, K.N. Sabharwal, T.G. Srinivasan, P.R.V. Rao, Kinetics of uranium extraction by macroporous bifunctional phosphinic acid resin, Solvent Extr. Ion Exch. 18 (2000) 551–565.

[73] M.W. Abdel Raouf, A.M. El-Kamash, Kinetics and thermodynamics of the sorption of uranium and thorium ions from nitric acid solutions onto a TBP-impregnated sorbent, J. Radioanal. Nucl. Chem. 267 (2006) 389–395.

[74] Z. Wen, K. Huang, Y. Niu, Y. Yao, S. Wang, Z. Cao, H. Zhong, Kinetic study of ultrasonic-assisted uranium adsorption by anion exchange resin, Colloids Surf., A 585 (2020), 124021.

[75] T. Kegl, A. Kosak, A. Lobnik, Z. Novak, A.K. Kralj, I. Ban, Adsorption of rare earth metals from wastewater by nanomaterials: a review, J. Hazard. Mater. 386 (2020), 121632.

[76] K.H. Chu, Revisiting the Temkin isotherm: dimensional inconsistency and approximate forms, Ind. Eng. Chem. Res. 60 (2021) 13140–13147.

[77] V. Puccia, M.J. Avena, On the use of the Dubinin-Radushkevich equation to distinguish between physical and chemical adsorption at the solid-water interface, Colloid Interface Sci. Commun. 41 (2021), 100376.

[78] G. Ye, J. Roques, P.L. Solari, C. Den Auwer, A. Jeanson, J. Brandel, L. J. Charbonnière, W. Wu, É. Simoni, Structural and thermodynamics studies on polyaminophosphonate ligands for uranyl decorporation, Inorg Chem 60 (2021) 2149–2159.

[79] H.N. Tran, E.C. Lima, R.-S. Juang, J.-C. Bollinger, H.-P. Chao, Thermodynamic parameters of liquid–phase adsorption process calculated from different equilibrium constants related to adsorption isotherms: a comparison study, J. Environ. Chem. Eng. 9 (2021), 106674.

[80] Y. Wang, X. Hu, Y. Liu, Y. Li, T. Lan, C. Wang, Y. Liu, D. Yuan, X. Cao, H. He, L. Zhou, Z. Liu, J.W. Chew, Assembly of three-dimensional ultralight poly (amidoxime)/graphene oxide nanoribbons aerogel for efficient removal of uranium (VI) from water samples, Sci. Total Environ. 765 (2021), 142686.

[81] L. Ding, T. Xiong, Z. Zhao, J. Liao, Y. Zhang, In-situ synthesis of Al_2O_3-TiO_2 nanocomposite with enhanced adsorption performance to uranium(VI) from aqueous solution, J. Mol. Liq. 362 (2022), 119731.

[82] X.T. Chen, L.F. He, R.Z. Liu, C. Zhang, B. Liu, Y.P. Tang, Effective uranium(VI) sorption from alkaline media using bi-functionalized silica-coated magnetic nanoparticles, RSC Adv. 5 (2015) 56658–56665.

[83] M. Zhang, M. Yuan, M. Zhang, M. Wang, J. Chen, R. Li, L. Qiu, X. Feng, J. Hu, G. Wu, Efficient removal of uranium from diluted aqueous solution with

hydroxypyridone functionalized polyethylene nonwoven fabrics, Radiat. Phys. Chem. 171 (2020), 108742.
[84] J. Huynh, R. Palacio, A. Allavena, H. Gallard, M. Descostes, A.-S. Mamède, S. Royer, E. Tertre, I. Batonneau-Gener, Selective adsorption of U(VI) from real mine water using an NH_2-functionalized silica packed column, Chem. Eng. J. 405 (2021), 126912.
[85] A.A. Galhoum, Facile synthesis of functionalized polyglycidyl methacrylate-magnetic nanocomposites for enhanced uranium sorption, RSC Adv. 9 (2019) 38783–38796.
[86] K. Philippou, I. Anastopoulos, C. Dosche, I. Pashalidis, Synthesis and characterization of a novel Fe_3O_4-loaded oxidized biochar from pine needles and its application for uranium removal. Kinetic, thermodynamic, and mechanistic analysis, J. Environ. Manage. 252 (2019), 109677.
[87] M.O. Abd El-Magied, A.A. Galhoum, A.A. Atia, A.A. Tolba, M.S. Maize, T. Vincent, E. Guibal, Cellulose and chitosan derivatives for enhanced sorption of erbium(III), Colloids Surf., A 529 (2017) 580–593.
[88] D. Yuan, Y. Wang, Y. Qian, Y. Liu, G. Feng, B. Huang, X. Zhao, Highly selective adsorption of uranium in strong HNO_3 media achieved on a phosphonic acid functionalized nanoporous polymer, J. Mater. Chem. A 5 (2017) 22735–22742.
[89] Z. Huo, S. Zhao, J. Yi, H. Zhang, J. Li, Biomass-based cellulose functionalized by phosphonic acid with high selectivity and capacity for capturing U(VI) in aqueous solution, Appl. Sci.-Basel 10 (2020) 5455.
[90] X. Liu, S. Hu, D. Xu, D. Shao, Removal of U(VI) from aqueous solution using carboxymethyl cellulose-modified Ca-rectorite hybrid composites, Korean J. Chem. Eng. 37 (2020) 776–783.
[91] J. Li, Y. Zhang, Y. Zhou, F. Fang, X. Li, Tailored metal-organic frameworks facilitate the simultaneously high-efficient sorption of UO_2^{2+} and ReO_4^- in water, Sci. Total Environ. 799 (2021), 149468.
[92] E. Nieboer, D.H.S. Richardson, The replacement of the non-descript therm heavy-metals by a biologically and chemically significant classification of metal-ions, Environ. Pollut. - Ser. B 1 (1980) 3–26.